Stem Cell Reports
Article
OPEN ACCESS

Huntingtin Regulates Mammary Stem Cell Division and Differentiation

Salah Elias,[1,2,3] Morgane S. Thion,[1,2,3] Hua Yu,[1,2,3] Cristovao Marques Sousa,[1,2,3] Charlène Lasgi,[1,2,3] Xavier Morin,[4,5,6] and Sandrine Humbert[1,2,3,*]
[1]Institut Curie, Orsay 91405, France
[2]CNRS UMR 3306, Orsay 91405, France
[3]INSERM U1005, Orsay 91405, France
[4]Ecole Normale Supérieure, Institut de Biologie de l'ENS, IBENS, Paris 75005, France
[5]INSERM U1024, Paris 75005, France
[6]CNRS UMR 8197, Paris 75005, France
*Correspondence: sandrine.humbert@curie.fr
http://dx.doi.org/10.1016/j.stemcr.2014.02.011

SUMMARY

Little is known about the mechanisms of mitotic spindle orientation during mammary gland morphogenesis. Here, we report the presence of huntingtin, the protein mutated in Huntington's disease, in mouse mammary basal and luminal cells throughout mammogenesis. Keratin 5-driven depletion of huntingtin results in a decreased pool and specification of basal and luminal progenitors, and altered mammary morphogenesis. Analysis of mitosis in huntingtin-depleted basal progenitors reveals mitotic spindle misorientation. In mammary cell culture, huntingtin regulates spindle orientation in a dynein-dependent manner. Huntingtin is targeted to spindle poles through its interaction with dynein and promotes the accumulation of NUMA and LGN. Huntingtin is also essential for the cortical localization of dynein, dynactin, NUMA, and LGN by regulating their kinesin 1-dependent trafficking along astral microtubules. We thus suggest that huntingtin is a component of the pathway regulating the orientation of mammary stem cell division, with potential implications for their self-renewal and differentiation properties.

INTRODUCTION

There are three distinct and differentially regulated stages in mammary gland development (embryonic, pubertal, and pregnancy/lactation), and the most substantial remodeling is postnatal (Gjorevski and Nelson, 2011). The mammary epithelium is organized into two cell layers: the luminal and basal myoepithelial layers. During pregnancy, the mammary gland completes its morphogenesis with the formation of alveolar buds where milk production is turned on at the end of pregnancy and during lactation (Silberstein, 2001). This developmental process is controlled by steroid hormones (Beleut et al., 2010). During lactation, luminal cells (LCs) produce and secrete milk, whereas basal myoepithelial cells (BCs) contract to release the milk from the nipple (Moumen et al., 2011).

Several lines of evidence indicate the existence of mammary stem cells (MaSCs) in mouse mammary tissue. These cells display the regenerative properties required for the substantial developmental changes in the adult mammary gland (Visvader and Lindeman, 2011). MaSCs have been isolated from adult mouse mammary tissue using the surface markers CD24 and β1 or α6-integrin chains (Shackleton et al., 2006). These populations are negative for steroid hormone receptors and consist of cells that express basal cell markers (Asselin-Labat et al., 2010). However, these populations appear to be composed of various subpopulations, ranging from multipotent stem cells to terminally differentiated luminal epithelial and myoepithelial cells (Visvader and Lindeman, 2011). Furthermore, the LC compartment itself is heterogeneous because progenitors of varying states of luminal differentiation and with diverse proliferative capacities can be identified (Shehata et al., 2012).

The importance of asymmetric cell divisions for stem cells/progenitors has been established in several tissues (Morin and Bellaïche, 2011; Shitamukai and Matsuzaki, 2012). In the mouse mammary gland, the reproductive cycle may alter the MaSC population by regulating the balance between symmetric and asymmetric divisions (Asselin-Labat et al., 2010; Joshi et al., 2010). Experimental perturbation of this balance results in abnormal epithelial morphogenesis and favors tumor growth (Cicalese et al., 2009; Taddei et al., 2008). Thus, MaSC divisions are important regulators of physiological and pathological stem cell biology. However, the precise molecular mechanisms underlying the division modes in mitotic MaSCs are still not understood.

The mitotic spindle is a key component of cell division. The position and orientation of the mitotic spindle are orchestrated by forces generated in the cell cortex (Grill and Hyman, 2005), where astral microtubules emanating from the mitotic spindle pole are tethered to the plasma membrane (Siller and Doe, 2009). Spindle orientation is determined by an evolutionarily conserved pathway, including cytoplasmic dynein, dynactin, the nuclear mitotic apparatus (NUMA) protein, and the G protein regulator leucine-glycine-asparagine repeat (LGN) protein (the

vertebrate homolog of *Caenorhabditis elegans* G protein-coupled receptor (GPR-1)/GPR-2 and *Drosophila* protein-protein interaction networks [PINS]) (Morin and Bellaïche, 2011). During cell division, LGN is recruited to the cell cortex through glycosyl phosphatidylinositol-linked $G_{\alpha i}/G_{\alpha o}$, which binds LGN carboxy-terminal GoLoco motifs (Zheng et al., 2010). Polarity cues restrict LGN localization to specific subcortical domains, where LGN recruits NUMA (Peyre et al., 2011). NUMA in turn interacts with microtubules and with the cytoplasmic dynein/dynactin complex. The precise localization of these interactions at the cell cortex ensures the positioning of the mitotic spindle through cortical capture of astral microtubules. Although these mechanisms have been well described in the skin and neuroepithelium, their involvement in the division of MaSCs is not known.

We previously showed that huntingtin (HTT), the protein mutated in Huntington's disease (HD), is required in murine neuronal progenitors for appropriate spindle orientation and for cell fate determination (Godin et al., 2010). Yet, the mechanisms underlying HTT function during spindle orientation remain unclear. HTT expression is not restricted to the brain: mutant HTT is detected in healthy mammary tissue and mammary tumors where it regulates tumor progression (Moreira Sousa et al., 2013). Thus, HTT may contribute to spindle orientation and cell fate choices outside the nervous system. Here, we investigated the function of HTT in mitosis of MaSCs during mouse mammary epithelium morphogenesis.

RESULTS

In Vivo Depletion of HTT from the Basal Compartment Leads to a Decreased Epithelial Content and Alters Self-Renewal of the Basal and Luminal Progenitors

We analyzed the expression pattern of wild-type HTT in mammary glands from virgin mice by immunohistochemistry. HTT immunoreactivity was observed in the basal and luminal compartments and increased as differentiation progressed (Figure 1A). We isolated basal and luminal epithelial cells from wild-type mice using flow cytometry (Figure S1A available online; Table S1). Evaluation of basal (*Krt14*) and luminal (*Krt18*) marker expression by quantitative real-time RT-PCR confirmed that BCs and LCs were found in the CD24-low/α6-high and CD24-high/α6-low fractions, respectively (Figure S1B). HTT was detected in BCs and LCs, but the signal was strongest in the luminal fraction (Figure 1B).

To test whether HTT regulates BC division and differentiation, we deleted HTT from the basal cell layer of the mammary epithelium by crossing $Htt^{flox/flox}$ mice harboring floxed *Htt* alleles (Dragatsis et al., 2000) with transgenic mice expressing *Cre* recombinase under the control of the keratin 5 (K5) promoter (Ramirez et al., 2004). *Cre* expression was mostly confined to the basal cell population (Figure S1C). We analyzed the distribution of HTT-deficient cells in mutant mammary epithelium by crossing K5*Cre*;$Htt^{flox/flox}$ mice with the *Rosa26-LacZ* reporter mouse strain (*R26*). At age 12 weeks, virtually all BCs were *LacZ* positive, whereas only 32% of LCs expressed *LacZ* (Figure 1C). The *LacZ*-negative LC population in the mutant epithelium may originate during early stages of gland development, from *LacZ*-negative BCs and from *LacZ*-negative cells committed to luminal differentiation that switched off the K5 promoter and escaped HTT deletion. Indeed, in embryonic day 18 (E18) K5*Cre*;$Htt^{flox/flox}$;*R26* embryos, a majority of cells in the central part of the developing mammary ducts did not express the *Cre* recombinase (Figure S1D). These cells expressed keratin 8 (K8) and were negative for K5, thus displaying luminal features (Figure S1E). Alternatively, the *LacZ*-negative LC population in the mutant epithelium may originate during adulthood from bipotent myoepithelial and luminal stem cells (Rios et al., 2014). *Htt* transcript levels were 79% lower in mutant than wild-type BCs (Figure 1D). In LCs from mutant mammary epithelium, *Htt* expression levels were 39% lower than the control value (Figure 1D).

Fewer epithelial cells could be isolated from the mutant than control mammary glands (Figures 1E and 1F). Also, the ratio between basal and LC populations was altered in mutant mammary epithelium (Figure 1G). We then performed a functional evaluation of progenitor cell content in control and mutant BCs using colony-formation assay. Mutant BCs formed significantly less colonies than control cells (0.84% ± 0.23% versus 3.32% ± 0.3%, Figure 1H). Similarly, the HTT-depleted LCs failed to form clonal colonies as compared to the control LC population (1.55% ± 0.72% versus 18.6% ± 2.3%, Figure 1I). Thus, K5-driven depletion of HTT leads to gland hypoplasia and affects colony-forming stem/progenitor populations in basal and luminal compartments.

HTT Is Required for Basal and LC Specification

We then analyzed the transcripts of genes associated with proliferation and myoepithelial and luminal lineages (Figure 2A; Table S1). The lower than control levels of the cell proliferation marker *Ki67* in BCs and LCs from mutant glands were consistent with the decrease in the overall population of epithelial cells. In the basal compartment in mutants, whereas *Krt18* was upregulated, *Krt14* and *Trp63* were differentially regulated with *Krt14* being increased and *Trp63* decreased (Figure 2A). In LCs from the mutant glands, both *Krt14* and *Trp63* were increased, whereas *Krt18* was decreased. Also, the expression levels of the

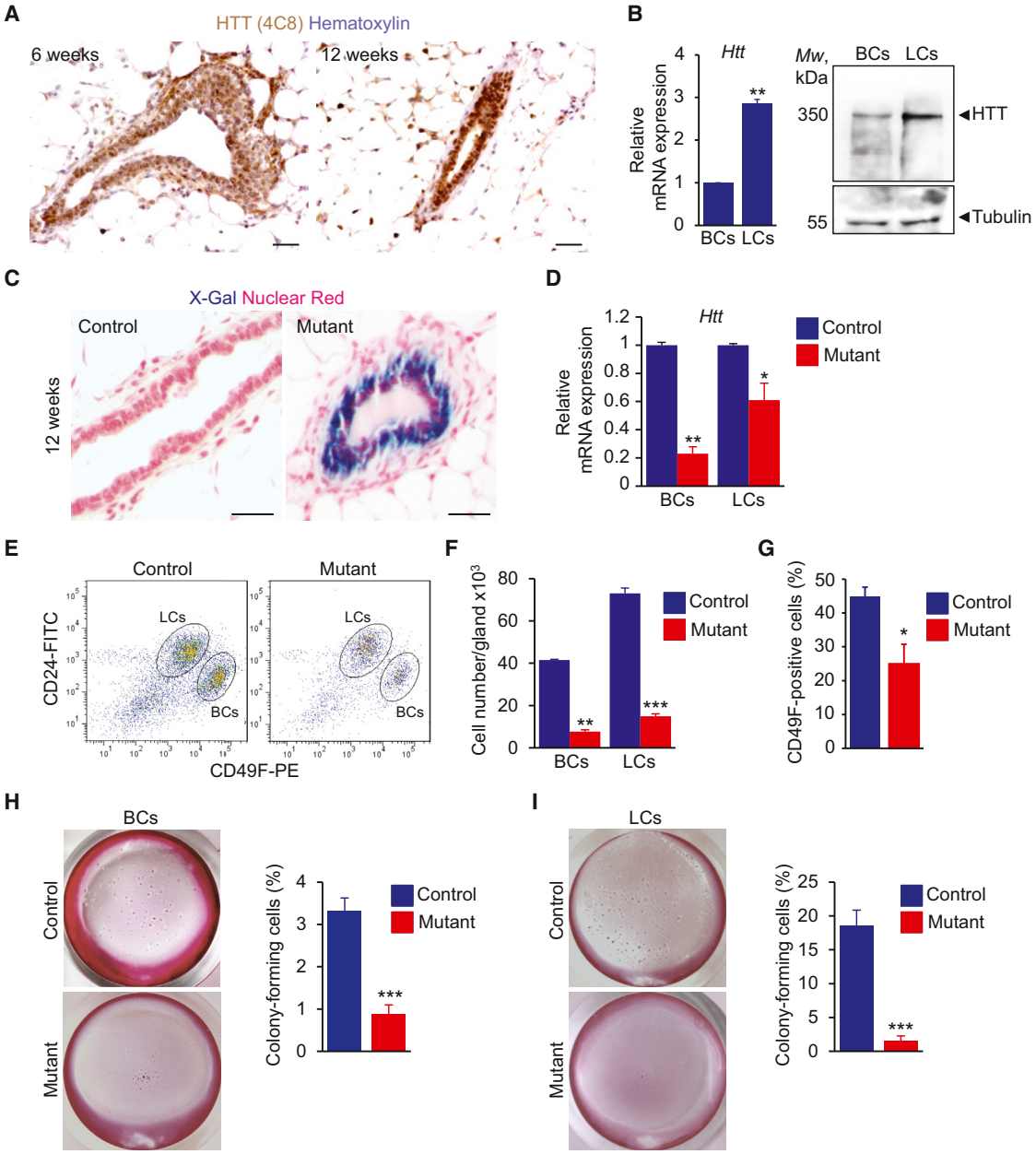

Figure 1. K5-Driven Loss of HTT Affects Basal and LC Populations

(A) Mammary gland sections from virgin C57Bl6/J mice stained for HTT.

(B) Quantitative real-time RT-PCR analysis of *Htt* gene and western blotting for HTT protein in basal and luminal mammary epithelial cells from 16-week-old virgin mice. Mw, molecular weight.

(C) *LacZ*-stained mammary gland sections from 12-week-old virgin control and mutant K5*Cre*;*Htt*$^{flox/flox}$;*R26* 12-week-old virgin mice.

(D) Quantitative real-time RT-PCR analysis of *Htt* gene expression in BCs and LCs from 16-week-old virgin mice.

(E) Representative dot plots showing separation of luminal ($CD31^-/CD45^-/CD24^+$/CD49F-low) and basal ($CD31^-/CD45^-/CD24^+$/CD49F-high) epithelial cells from 16-week-old virgin mouse mammary glands by flow cytometry.

(F) Number of BCs and LCs isolated per gland of 16-week-old virgin mice.

(G) Percentages of CD49F-high cells in $CD45^-/CD31^-/CD24^+$ cell populations.

(H and I) Colonies formed by BCs (H) and LCs (I) isolated from mammary glands of 16-week-old virgin mice.

Scale bars, 50 μm (A and C). Error bars, SEM.*p < 0.05; **p < 0.01; ***p < 0.001. See also Figure S1 and Table S1.

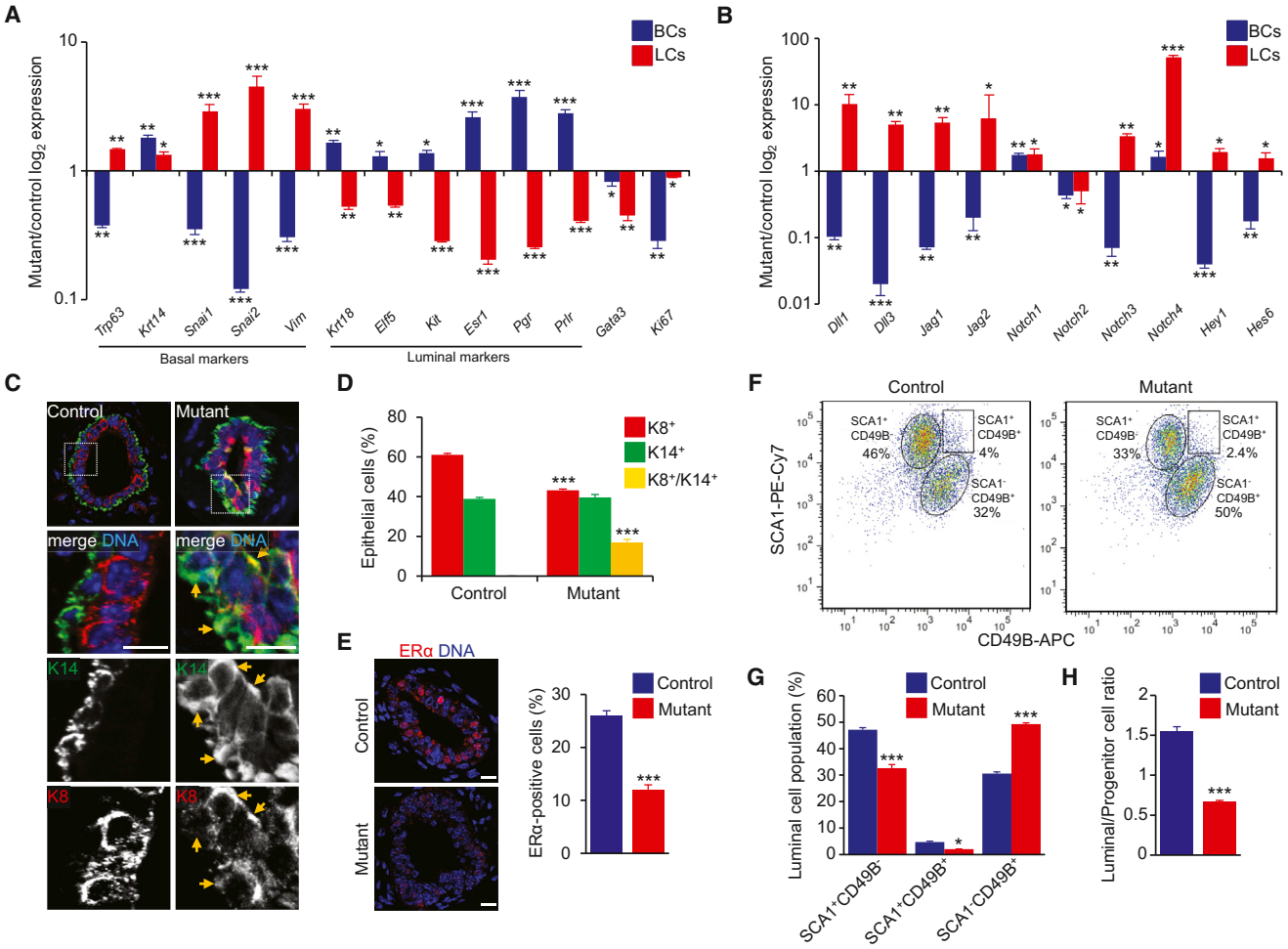

Figure 2. Loss of HTT Alters Basal to Luminal Specification

(A and B) Quantitative real-time RT-PCR analysis of the indicated genes in BCs and LCs from 16-week-old mice.

(C) Sections from 12-week-old mammary glands stained for K14 and K8. Arrows point to $K8^+K14^+$ epithelial cells.

(D) Percentage of $K8^+$, $K14^+$, and $K8^+K14^+$ cells.

(E) Sections from 12-week-old mammary glands stained for ERα. Right panel shows the percentages of ERα-positive cells.

(F) Representative dot plots showing the frequency of $SCA1^+$ and $CD49B^+$ cells in the LC population in 16-week-old virgin mice.

(G) Percentages of $SCA1^+CD49B^-$, $SCA1^+CD49B^+$, and $SCA1^-CD49B^+$ cells.

(H) Ratio of $SCA1^+CD49B^-$-to-$SCA1^-CD49B^+$ cells.

Scale bars, 10 μm. Error bars, SEM.*p < 0.05; **p < 0.01; ***p < 0.001. See also Table S1.

epithelial-to-mesenchymal transition (EMT)-related genes (*Snai1*, *Snai2*, and *Vim*) were decreased in mutant BCs and increased in mutant LCs as compared to control cells (Figure 2A). We tested luminal markers: mutant LCs displayed a marked decrease in the expression levels of mature LC genes (*Esr1*, *Pgr*, and *Prlr*) as compared to control cells (Figure 2A). The expression levels of *Elf5* and *Kit* transcripts that are markers of the luminal progenitor-enriched population were also significantly lower in mutant LCs than in control. This was sustained by the decreased expression of the transcription factor *Gata3* in mutant BCs and LCs (Figure 2A). Finally, mutant BCs expressed higher levels of luminal markers as compared to control cells (Figure 2A). Thus, the K5-driven loss of HTT affects the proliferative potential and the identity of BC and LC populations.

NOTCH signaling is involved in cell fate determination in the mammary epithelium (Bouras et al., 2008; Yalcin-Ozuysal et al., 2010). We thus assayed the mRNAs of the *Notch* ligands (*Dll1*, *Dll3*, *Jag1*, and *Jag2*), the *Notch1–Notch4* receptors, and the *Hey1* and *Hes6* target genes (Figure 2B). The NOTCH pathway was downregulated in BCs and overactivated in LCs from mutant mice, relative to controls. Immunohistochemical labeling of 12-week-old mammary glands for K14 and K8 further confirmed that

basal and luminal specifications were altered in HTT-deficient mice (Figure 2C). HTT-depleted mammary ducts exhibited an unusual expansion of $K14^+K8^+$ double-positive cells (17.2% ± 1.32%, Figure 2D).

The overall increase in NOTCH signaling in the luminal compartment suggested that the absence of HTT may inhibit LC fate acquisition. Indeed, the proportion of estrogen receptor (ER) α-expressing cells decreased in mutant epithelia as compared to controls (Figure 2E). We next analyzed the luminal subpopulations by flow cytometry based on the expression of CD49B and SCA1 (Figures 2F and 2G). The $SCA1^+CD49B^-$ population consists of mature LCs, whereas the $SCA1^-CD49B^+$ cells are luminal progenitor cells (Shehata et al., 2012). A high proportion of the luminal population in control epithelium was $SCA1^+CD49B^-$ (47.2% ± 0.8% versus 30.6% ± 0.6% for the $SCA1^-CD49B^+$ population). In mutant conditions, the $SCA1^-CD49B^+$ luminal subpopulation was much larger (49.3% ± 0.4% versus 32.6% ± 1.3% for the $SCA1^+CD49B^-$ population). Accordingly, the ratio of mature LCs to progenitors was lower in the mutant luminal fraction as compared to controls (Figure 2H). This indicates that K5-driven HTT depletion decreases the capacity of the basal and luminal compartments to properly commit to a myoepithelial or LC fate.

HTT Regulates Mammary Epithelial Morphogenesis during Pregnancy and Lactation

We investigated differentiation of mammary glands on day 18.5 of pregnancy and day 1 of lactation when HTT was strongly expressed (Figure S2A). There were fewer secretory alveoli in mutant than control glands, and the epithelial content was lower (Figures 3A and 3B). Notably, there were fewer well-developed alveoli in mutant than control glands. This was confirmed by analysis of *lacZ* reporter expression in K5*Cre*;*Htt*$^{flox/flox}$;*R26* mammary glands (Figure S2B). On day 7.5 of pregnancy, most LCs in ducts and alveolus-like structures in mutant glands stained blue with X-gal, with only a few *lacZ*-negative cells detected. The number of *lacZ*-negative cells was higher during pregnancy and lactation; also, on day 1 of lactation, the well-differentiated newly formed alveoli were *lacZ* negative (Figure S2B).

On day 18.5 of pregnancy and day 1 of lactation, KI67 labeling indicated a higher rate of proliferation for mutant than control alveolar cells (Figure S2C). The formation of the lumen involves apoptosis, which was also affected by HTT depletion. On day 14.5 of pregnancy, there were more cells but less apoptosis in the lumen of mutant than control glands (data not shown). On day 18.5 of pregnancy and day 1 of lactation when the lumens are fully generated, there was no detectable apoptosis in controls (Figure S2D). In contrast, mutant alveoli still displayed cleaved caspase-3-positive cells in their lumen, suggesting a delay in lumen formation.

On day 18.5 of pregnancy, the mutant alveoli were poorly differentiated, containing few milk droplets (Figure 3A). In controls, the large cytoplasmic lipid droplets in the luminal alveolar cells on day 18.5 of pregnancy were replaced by small lipid droplets at the luminal surface on day 1 of lactation. In mutant mammary glands, the large cytoplasmic droplets remained in the alveolar cells on day 1 of lactation (Figure 3B, arrows), indicating secretory dysfunction. We investigated the subcellular localization of signal transducer and activator of transcription 5A (STAT5A) on 1 day of lactation (Figure 3C). Upon activation by prolactin, nuclear phosphorylated STAT5A (p-STAT5A) regulates the expression of genes involved in lobulo-alveolar differentiation and lactation (Jahchan et al., 2012). Mutant alveolar cells displayed less nuclear p-STAT5A than control glands. Consistent with this, the milk Whey acid protein (WAP) immunolabeling and the levels of the RNAs for the milk proteins β-casein (*Csn2*) and WAP (*Wap*) were lower in mutant than control glands (Figure 3D).

Because the overall architecture of mutant glands showed abnormalities, we tested whether epithelial cell polarity was affected. We analyzed the localization of ZO1 (*zonula occludens* 1), PAR3 (Partitioning Defective 3), aPKC (atypical protein kinase C), and E-cadherin in LCs on 18.5 day of pregnancy (Figure 3E). In control glands, PAR3 and ZO1 colocalized at the tight junctions of LCs, whereas in mutant alveoli, the labeling was more diffuse, and PAR3 accumulated in the cytoplasm (Figure 3E). E-cadherin, which was enriched at the lateral compartment in control LCs, accumulated with aPKC at the apical surface of mutant cells (Figure 3E). $K8^+$ LCs were distinguishable from $K14^+$ BCs in control alveoli, whereas both K8 and K14 immunoreactivities showed substantially abnormal patterns in mutant glands (Figure 3F). Thus, the absence of HTT alters morphological and functional differentiation, epithelial polarization, and milk production during alveologenesis.

HTT Controls Mitotic Spindle Orientation in Mouse Mammary Basal Cells

Next, we addressed potential mechanisms by which HTT may regulate mammary gland morphogenesis. HTT regulates the mitotic spindle positioning in mouse neuronal progenitors (Godin et al., 2010). We analyzed the division of BCs in ducts from the outgrowths that developed on day 7.5 of pregnancy when the stimuli of pregnancy induce basal cell division to ensure mammary gland growth (Taddei et al., 2008). HTT was observed at the spindle poles during metaphase and at the cortical area in metaphase and anaphase (Figure 4A). Similarly to what is

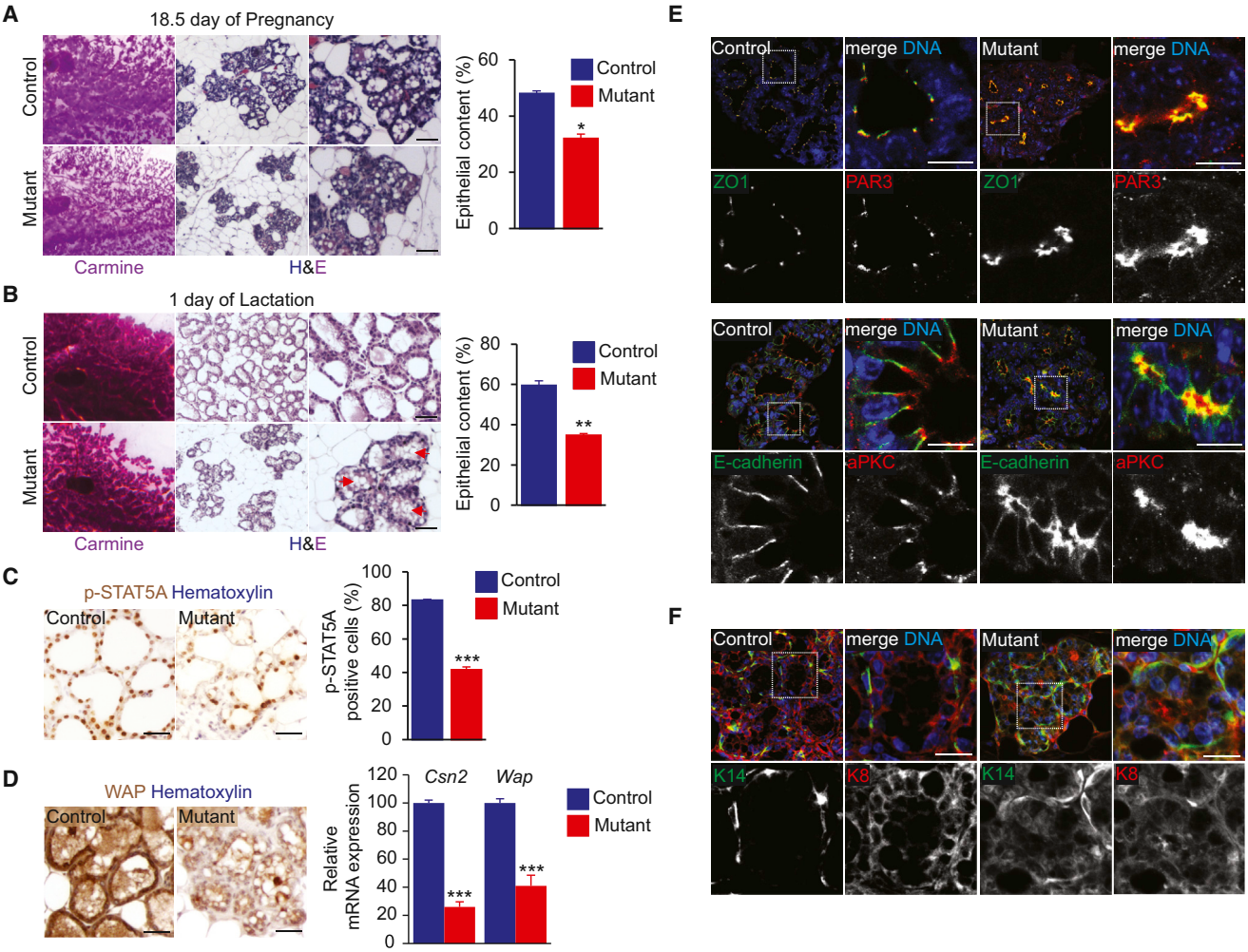

Figure 3. HTT Is Required for Epithelial Morphogenesis during Pregnancy and Lactation

(A and B) Carmine-stained whole mounts of mammary glands and hematoxylin and eosin staining (H&E) at low (middle) and high (right) magnifications. The histograms show the quantification of the epithelial content.

(C) Mammary gland sections stained for p-STAT5A and percentages of p-STAT5A-positive cells.

(D) Mammary gland sections from 1-day lactating mice stained for WAP and quantitative real-time RT-PCR analysis of *Csn2* and *Wap* gene expression.

(E and F) Mammary gland sections from 18.5-day pregnant mice stained as indicated. Scale bars, 10 μm.

Scale bars, 50 μm (A–D). Error bars, SEM. *p < 0.05; **p < 0.01; ***p < 0.001. See also Figure S2.

observed in cultured cells (below) (Godin et al., 2010), HTT labeling was also present at the spindle midbody area during anaphase and telophase.

In dividing epithelial cells, the mitotic spindle undergoes a rapid phase of rotation during early metaphase until it reaches a planar orientation, followed by a longer phase of planar maintenance until anaphase onset (Peyre et al., 2011). We evaluated the orientation of the mitotic spindle during metaphase and telophase (Figures 4B and 4C). In control BCs, most metaphase and telophase cells (71% and 74%, respectively) displayed spindle angles between 0° and 15° (planar/horizontal division) (Figures 4D–4F). The spindle angles were randomized in mutant BCs, with a majority of cells displaying oblique and vertical divisions. These findings indicate that HTT is required for correct spindle orientation in dividing mammary BCs.

HTT Modulates Mitotic Spindle Orientation in Mammary Epithelial Cells in a Dynein-Dependent Manner

We used human basal-like MCF-10A mammary cells to investigate the mechanisms underlying the function of HTT in spindle orientation. Cells were transfected with si-Control, si-HTT1 targeting HTT, or si-dynein targeting the

heavy chain of the dynein complex (Figure 4G). The amount of HTT at the spindle poles was affected by both small interfering RNAs (siRNAs) (Figure 4H). We analyzed the position of the spindle poles with respect to the substratum plane (Figures S3A, S3B, and 4I). In control cells, virtually all spindles were parallel to the substratum plane (3.5° ± 0.2°) (Figure 4I). In contrast, most HTT-depleted and dynein-depleted cells failed to align their spindle with the substratum plane (16.5° ± 0.4° and 20.3° ± 0.6°, respectively) (Figure 4I).

We also reduced HTT levels using si-HTT2, whose target sequence in HTT is different from that of si-HTT1 (Figure 4J). Again, a misoriented spindle was observed following the use of si-HTT2 (Figure 4K). Next, we introduced a construct encoding a full-length HTT (HTTFL; Figures 4J) (Pardo et al., 2010). si-HTT2 was designed to inhibit the expression of endogenous HTT but had no effect on the expression of the HTTFL construct (Figure 4J) (Pardo et al., 2010). Expression of the HTTFL restored the spindle orientation defect caused by si-HTT2 to the control situation (Figures 4K and S3A).

HTT interacts with dynein in neurons (Caviston et al., 2007; Gauthier et al., 2004), so HTT and dynein may act together to regulate spindle orientation. We depleted endogenous HTT using si-HTT2 and expressed a variant of HTTFL devoid of its dynein-interacting domain (HTTΔDYN) and unable to bind dynein (Pardo et al., 2010) (Figure 4J). HTTΔDYN was mislocalized from the spindle poles (Figures 4L and S3A) and failed to rescue the spindle orientation defect induced by si-HTT2 (Figures 4K and S3A).

We also investigated cell-cycle progression by video recording cells stably expressing fluorescent histone 2B (Cherry) and α-tubulin (GFP) (Figure S3C; Movies S1 and S2). The duration of mitosis was similar in si-HTT1-transfected and control cells (Figure S3C), although HTT depletion led to an alteration in spindle orientation (Figures S3C–S3E). Notably, the spindle angles measured from live-imaging data were higher than those from fixed-cell samples (Figures 4I, 4K, and S3D). Possibly, the angle can be underestimated in fixed samples due to drying effects causing flattening of the sample. These observations show that HTT regulates spindle orientation in mammary cells by a mechanism that involves its interaction with dynein.

HTT Forms a Complex with Dynein/Dynactin/NUMA/LGN in Dividing Mammary Epithelial Cells

We investigated the nature of the molecular machinery involved in the function of HTT during spindle orientation. During interphase, HTT showed a punctate distribution in the cytosol (Figure 5A). During mitosis from prophase to late anaphase, spindle poles became enriched in HTT. HTT displayed punctate staining beneath the cellular cortex reminiscent of astral microtubules plus ends at prometaphase and metaphase. HTT was also present at the spindle midzone during anaphase and telophase (Figure 5A). Other anti-HTT antibodies gave similar findings (Figure S4A).

The dynein/dynactin complex is required for the assembly of the spindle, and it is also essential at the cell cortex to exert pulling forces on astral microtubules (Morin and Bellaïche, 2011). LGN is necessary for planar spindle orientation (Konno et al., 2008; Morin et al., 2007). To study the localization of HTT, P150^{Glued}, dynein, NUMA, and LGN at the spindle and cellular cortex, we used a fixation procedure including incubation in anhydrous methanol containing 2% paraformaldehyde to maintain the integrity of microtubules emanating from the spindle poles (Figure 5B). We found that HTT colocalized with P150^{Glued}, dynein, and NUMA at the spindle and spindle poles (Figure 5B). HTT, P150^{Glued}, dynein, and NUMA were also detected on astral microtubules and microtubule plus ends. LGN formed a typical crescent shape at the cell cortex and colocalized with HTT at the spindle pole (Figure 5B). Immunoprecipitation of HTT from MCF-10A cells synchronized at metaphase led to the coimmunoprecipitation of NUMA, P150^{Glued}, dynein, and LGN (Figure 5C). However, $G_{\alpha i}/G_{\alpha o}$ did not coimmunoprecipitate with HTT (Figure S4B). Because $G_{\alpha i}/G_{\alpha o}$ localization is restricted to the cell cortex, this suggests that HTT is not stably associated with the cell cortex. Thus, HTT is part of the dynein/dynactin/NUMA/LGN complex at the spindle poles and along astral microtubules and may regulate its microtubule-based delivery from the spindle poles to the cell cortex (Figure 5D).

HTT Is Required for the Cortical Localization of Dynein, Dynactin, NUMA, and LGN during Mitosis

We analyzed the influence of HTT on the mitotic localization of NUMA, P150^{Glued}, dynein, and LGN. NUMA colocalized with P150^{Glued}, dynactin, and LGN at the spindle poles and formed cortical crescents facing the spindle poles during metaphase (Figure 6A). HTT depletion affected the localization of P150^{Glued}, dynein, NUMA, and LGN: these proteins relocalized from the cell cortex to accumulate at the spindle poles (Figures 6A–6D). Expression of the HTTFL restored the cortical distribution defect of P150^{Glued}, dynein, NUMA, and LGN caused by si-HTT2 to the control situation (Figures S5A–S5D). However, HTTΔDYN failed to do so. We then analyzed the distribution of HTT partners in vivo in control and HTT-depleted dividing BCs. HTT depletion resulted in fewer BCs displaying cortical accumulation of NUMA (27% ± 5.1% versus 73% ± 2.6%) and LGN (21% ± 3.3% versus 68% ± 4.7%) during metaphase (Figure 6E). These data implicate HTT in the delivery of

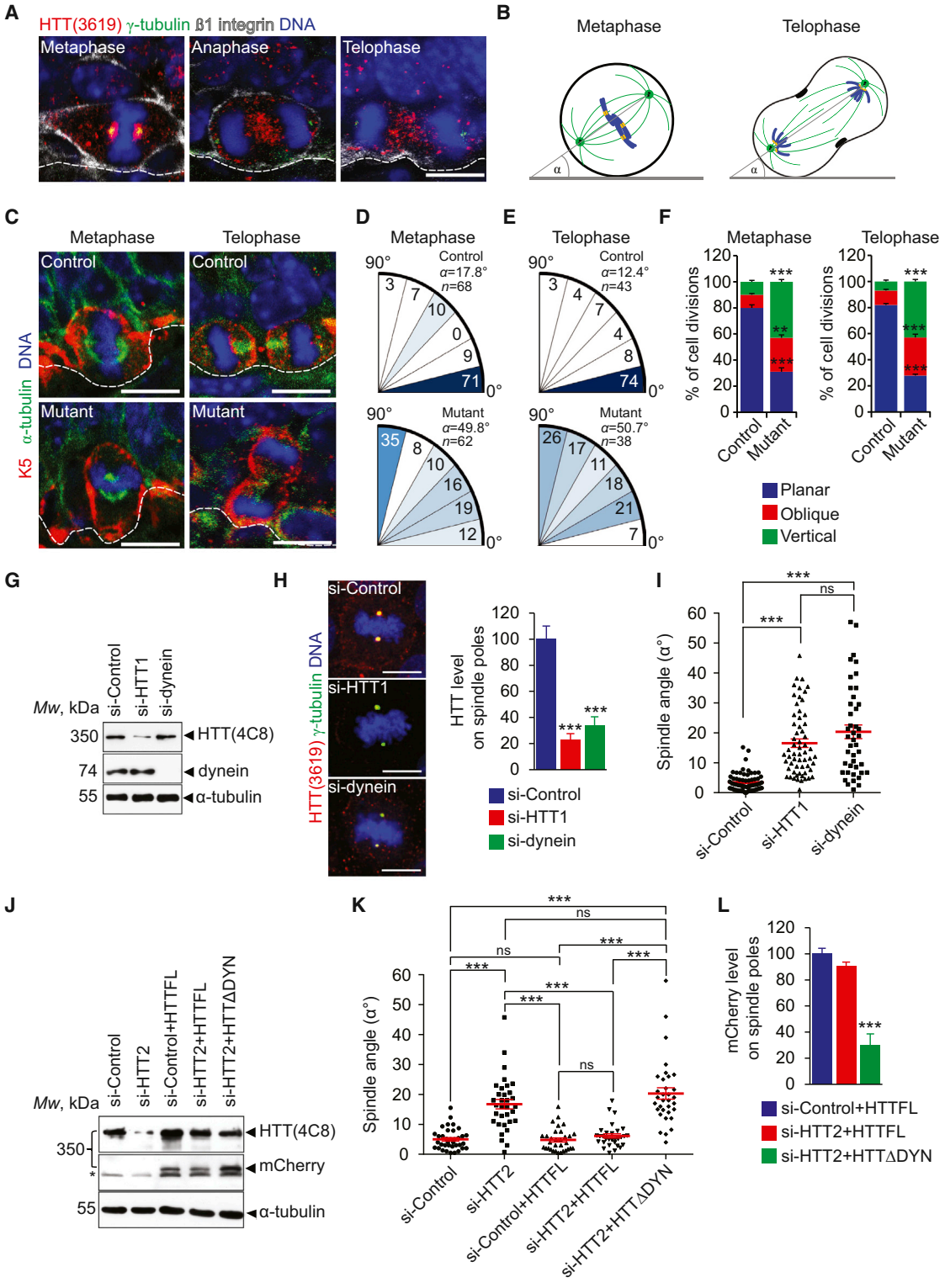

Figure 4. HTT Regulates Mitotic Spindle Orientation in Basal Cells in a Dynein-Dependent Manner

(A) Mammary gland sections from 7.5-day pregnant mice.

(B) Schemes illustrating measurement of the spindle angle α.

(C) Mammary gland sections from 7.5-day pregnant mice.

(legend continued on next page)

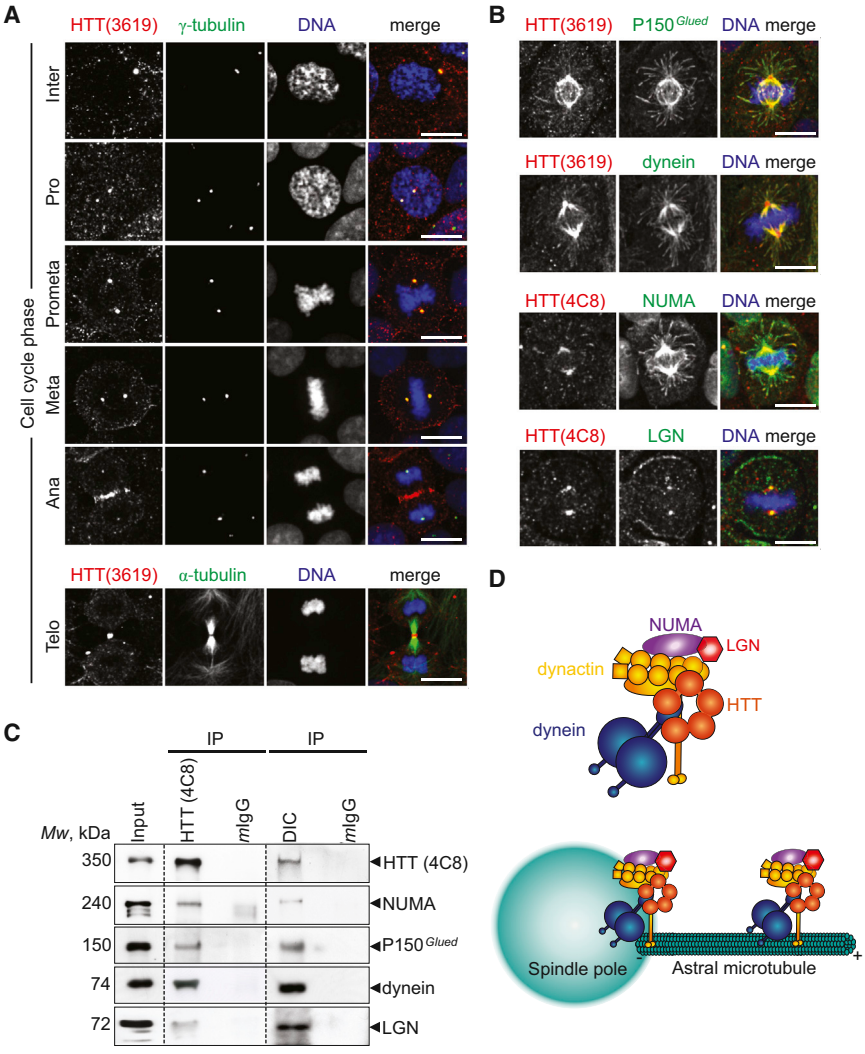

Figure 5. HTT Codistributes with Dynein/Dynactin/NUMA/LGN

(A and B) Mammary cells stained as indicated. Scale bars, 10 μm. Telo, telophase; Ana, anaphase; Meta, metaphase; Prometa, prometaphase; Pro, prophase; Inter, interphase.

(C) HTT/dynein/dynactin/NUMA/LGN complexes were immunoprecipitated from cells arrested in metaphase before lysis. Mouse IgG (*m*IgG) was used as a negative control. The immunoprecipitates (IP) were analyzed by western blotting.

(D) Cartoon showing the HTT/dynein/dynactin/NUMA/LGN complex at the spindle pole and on astral microtubules in metaphase cells.

See also Figure S4.

P150^{Glued}, dynein, NUMA, and LGN to the cell cortex during mitosis.

To confirm this possibility, we performed live-cell imaging of HeLa cells stably expressing the dynein heavy chain or LGN fused to GFP (DHC-GFP and GFP-LGN; Figure 6F; Movies S3, S4, S5, and S6). During mitosis, dynein oscillates from one pole of the cell cortex to the other, generating asymmetric forces that center the spindle (Kiyomitsu and Cheeseman, 2012). In control cells, DHC-GFP was distributed asymmetrically with respect to both the cell cortex and the mitotic spindle during metaphase, and then relocalized symmetrically at anaphase onset, until telophase (Figures 6F and 6G). HTT depletion impaired the dynamics of DHC-GFP localization at the cell cortex, and the

(D and E) Spindle angles of basal cells; values are expressed as a percentage of basal cells within each interval. Mean angle and number of measures (n) are shown.

(F) Percentages of planar (0°–30°), oblique (30°–60°), and vertical (60°–90°) divisions.

(G) Western blotting of mammary cell extracts.

(H) HTT abundance at spindle poles (right).

(I) Distribution and mean spindle angle in metaphase mammary cells.

(J) Western blotting of cell extracts. The star indicates a contaminating band.

(K) Distribution and mean spindle angles in metaphase mammary cells.

(L) HTT (mCherry) labeling at spindle poles in metaphase mammary cells.

Scale bars, 10 μm. Error bars, SEM. ns, not significant. **p < 0.01. ***p < 0.001. See also Figure S3.

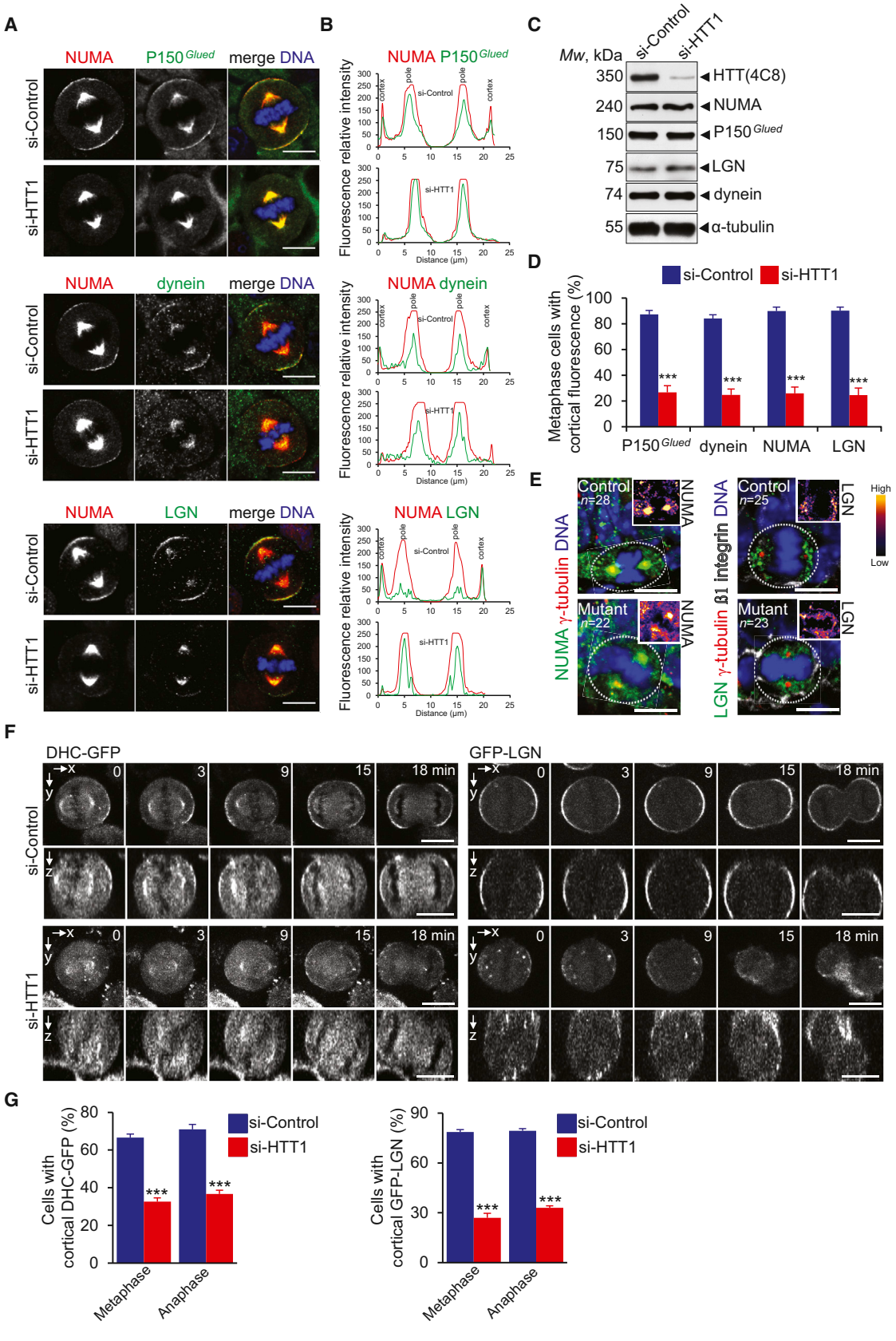

(legend on next page)

proportion of HTT-depleted cells displaying cortical DHC-GFP was low in metaphase (32.7% ± 2.6% versus 66.7% ± 1.8% for controls) and anaphase (36.7% ± 2.1% versus 71% ± 1.9%). Remarkably, cortical accumulation of GFP-LGN was decreased in HTT-depleted cells compared to control cells where GFP-LGN formed a bipolar cortical crescent from metaphase to anaphase (Figure 6F). The proportions of cells displaying cortical accumulation of GFP-LGN in metaphase and anaphase were lower in si-HTT-transfected than control cells (27% ± 2.7% versus 78.7% ± 1.4% and 33% ± 1.1% versus 79.3% ± 1.3%) (Figure 6G). These effects were confirmed by z stack analysis (Figure 6F). We conclude that HTT regulates the dynamics of the dynein/dynactin/NUMA/LGN complex, therefore ensuring its cortical localization.

HTT-Mediated Transport of the Dynein/Dynactin/NUMA/LGN Complex from the Spindle Poles to the Cell Cortex Involves Kinesin 1

HTT interacts with kinesin 1 (KIF5) through the huntingtin-associated protein 1 (HAP1) to promote microtubule-based anterograde vesicular transport in neurons (Colin et al., 2008; Gauthier et al., 2004; McGuire et al., 2006; Shirasaki et al., 2012). Furthermore, HTT transports brain-derived neurotrophic factor (BDNF) vesicles in an anterograde manner, and BDNF anterograde transport depends specifically on kinesin 1, and not kinesin 2 (Dompierre et al., 2007; Gauthier et al., 2004). We hypothesized that kinesin 1 could mediate the HTT-dependent anterograde transport of P150^{Glued}, dynein, NUMA, and LGN from the spindle poles to the cell cortex. HTT colocalized with kinesin 1 on the spindle poles, mitotic spindle, and astral microtubules in metaphase cells (Figure 7A). Immunoprecipitation of HTT from metaphase-synchronized MCF-10A cells led to the coimmunoprecipitation of kinesin 1 (Figure 7B). HTT depletion impaired the recruitment of kinesin 1 on the spindle poles and astral microtubules (Figures 7C–7E). Conversely, si-kinesin 1 treatment altered the localization of P150^{Glued}, dynein, and NUMA on astral microtubules and that of LGN at the cell cortex (Figures 7F–7I).

Finally, we tested whether the recruitment of P150^{Glued}, dynein, NUMA, and LGN to the cell cortex was microtubule dependent by treating cells with 40 nM of nocodazole to disrupt astral microtubules (data not shown). Disruption of astral microtubules altered the recruitment of HTT, P150^{Glued}, dynein, NUMA, and LGN to the spindle poles (Figures S6A–S6D) and of P150^{Glued}, dynein, NUMA, and LGN to the cell cortex (Figures S6C and S6E). In the majority of the cells still displaying cortical LGN, LGN was distributed more randomly on the entire cell cortex and not restricted to a bipolar cortical crescent facing the poles as in the control situation (Figures S6C and S6F). This indicates that astral microtubules are required for the establishment of the bipolar symmetrical cortical distribution of LGN during metaphase. Together, these findings support the idea that HTT regulates the dynamics of the dynein/dynactin/NUMA/LGN complex along astral microtubules through kinesin 1 (Figure 7J).

DISCUSSION

Our studies shed light on the role of HTT as a modulator of the mammary epithelial morphogenesis and of spindle orientation in MaSCs. HTT is not only crucial for spindle pole assembly but also for the cortical localization of the dynein/dynactin/NUMA/LGN complex. HTT may be a molecular link between the dynein/dynactin and NUMA/LGN pathways ensuring the transport of the dynein/dynactin/NUMA/LGN complex from the spindle pole to the cell cortex. Indeed, we identify kinesin 1 as a molecular plus-end motor regulating the trafficking of the dynein/dynactin/NUMA/LGN complex to the cell cortex during mitosis. We propose a model in which HTT regulates MaSC division through this complex, with consequences for self-renewal and tissue cell fate specification and architecture. However, this does not exclude that HTT may also affect mammary gland morphogenesis by impairing directly luminal differentiation.

In vertebrates, a correlation between spindle orientation and the acquisition of cell fate has been proposed for the division of skin progenitors (Williams et al., 2011) and neuronal radial glial cells (reviewed in Morin and Bellaïche, 2011; Peyre and Morin, 2012; Shitamukai and Matsuzaki, 2012). This proposal is based on the observation that a loss of function of several proteins known to control

Figure 6. Loss of HTT Prevents Cortical Accumulation of Dynein-Dynactin-NUMA-LGN during Mitosis

(A) Mammary cells stained as indicated.
(B) Line-scan analysis (relative fluorescence intensity).
(C) Western blotting of cell extracts.
(D) Percentage of cells with cortical accumulation of dynein, P150^{Glued}, NUMA, and LGN.
(E) Mammary gland sections from 7.5-day pregnant mice. Gradients of color intensity were applied to NUMA and LGN stainings (insets).
(F) DHC-GFP and GFP-LGN HeLa cells were video recorded. Maximum intensity and z projections are shown.
(G) Percentage of HeLa cells with cortical accumulation of DHC and LGN.
Scale bars, 10 μm. Error bars, SEM. ***p < 0.001. See also Figure S5 and Movies S3, S4, S5, and S6.

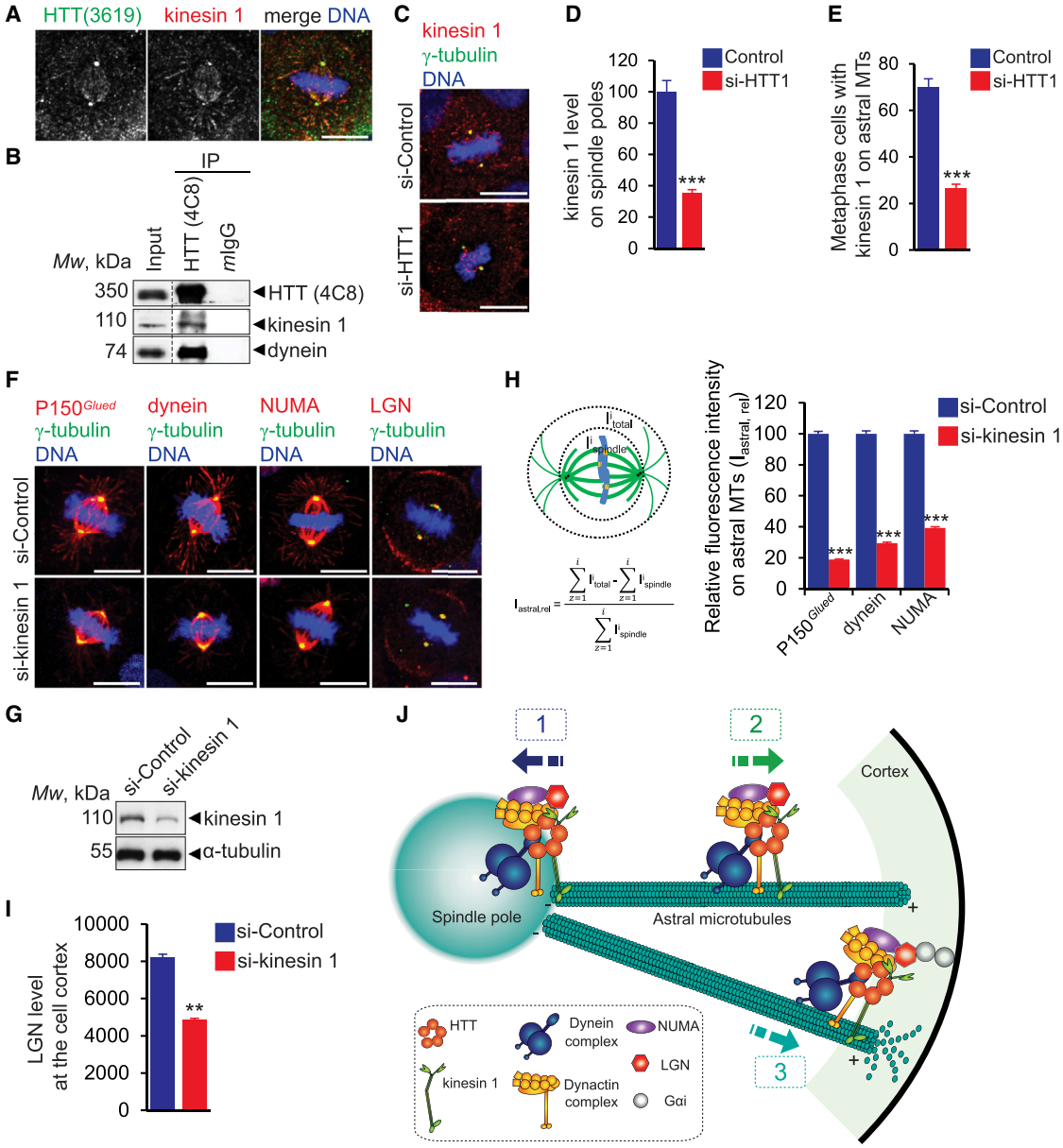

Figure 7. Kinesin 1 Participates in HTT-Mediated Cortical Localization of the Dynein/Dynactin/NUMA/LGN Complex during Mitosis

(A) Mammary cells stained as indicated.

(B) HTT/dynein/kinesin 1 complexes were immunoprecipitated from cells arrested in metaphase before lysis. Mouse IgG (*m*IgG) was used as a negative control. The immunoprecipitates were analyzed by western blotting.

(C) Mammary cells stained as indicated.

(D) Kinesin 1 abundance at spindle poles.

(E) Percentages of cells with kinesin 1 on astral microtubules.

(F) Mammary cells stained as indicated.

(G) Western blotting of cell extracts.

(H) Quantification of the relative fluorescence intensities of P150^{Glued}, dynein, and NUMA on astral microtubules. The intensities of the spindle ($I_{spindle}$) and of the total cell (I_{total}) were determined with ImageJ software. Relative intensities on astral microtubules ($I_{astral,\ rel}$) were calculated, and control value was set to 100.

(I) LGN abundance at the cell cortex.

(legend continued on next page)

spindle orientation also leads to early differentiation. However, disruption of the LGN complex causes spindle randomization with little effect on differentiation (Konno et al., 2008; Morin et al., 2007; Peyre et al., 2011), suggesting that spindle orientation and fate choices may be regulated in parallel, rather than there being a causal relationship between them. During mammary gland maturation, MaSCs amplify their pool through symmetric divisions, and then switch to a differentiation phase during which they divide asymmetrically to produce a more committed daughter cell (Joshi et al., 2010). Spindle orientation may be a mechanism controlling the balance between symmetric and asymmetric division (Joshi et al., 2010; Regan et al., 2013; Taddei et al., 2008). We observed that deletion of HTT from the basal compartment reduced the global epithelial content as a result of the decrease in the pool of MaSCs. However, the randomization of spindle orientation did not accelerate final LC fate commitment but favored an intermediate luminal progenitor cell status. Our study thus provides further support for the idea that spindle orientation is instrumental for planar division and the maintenance of the pool of cells ensuring self-renewal. The influence of spindle orientation on cell fate specification may be less clear cut and depend on different factors including the nature of the epithelium and the developmental stage.

How can mitotic spindle orientation affect cell fate acquisition in the mammary gland? A recent study showed that Aurora A kinase regulates the orientation of the mitotic spindle and the location of the postmitotic cells, thereby influencing LC fate determination (Regan et al., 2013). The authors propose that Aurora A kinase favors planar divisions through active NOTCH signaling. We show that a loss of HTT impairs NOTCH signaling during LC fate determination. HTT is essential for the cortical localization of dynein/dynactin/NUMA/LGN. In mouse embryonic skin progenitors, the loss of LGN, NUMA, and dynactin impairs asymmetric division and inhibits NOTCH signaling, leading to defects in morphogenesis (Williams et al., 2011). In addition to its role in spindle orientation, HTT may also affect NOTCH signaling through the regulation of its inhibitor NUMB that plays a role in asymmetric cell divisions (Lancaster and Knoblich, 2012). In *Drosophila*, NUMB interacts with the PAR3-PAR6-aPKC polarity complex promoting NOTCH activation. HTT is found in complex with PAR3 and aPKC (Shirasaki et al., 2012) and could thus regulate their cortical localization with a consequent effect on NOTCH signaling. Alternatively, HTT may act on NOTCH signaling through a mechanism involving endocytosis: HTT regulates endocytosis (Caviston et al., 2007; Velier et al., 1998), and NUMB and Adaptor Protein complex 1 and 2 (AP-1 and AP-2) are found in complex with HTT (Shirasaki et al., 2012). In fact, in *Drosophila*, NUMB antagonizes NOTCH signaling by influencing the recycling of NOTCH complexes via AP-1 and AP-2 (Cotton et al., 2013; Couturier et al., 2013).

HTT forms a complex with dynein and dynactin in neurons to promote axonal microtubule-based vesicular transport (Caviston et al., 2007; Gauthier et al., 2004). Here, we demonstrate that HTT regulates spindle orientation through its interaction with dynein. Dynein and dynactin are recruited to the cell cortex by the $G_{\alpha i}/G_{\alpha o}$-LGN-NUMA complex where they generate pulling forces that control spindle position and orientation (Kiyomitsu and Cheeseman, 2012; Kotak et al., 2012; Woodard et al., 2010). During metaphase, a signal comprising the spindle pole-localized polo-like kinase 1 (PLK1) regulates dynein localization by controlling the interaction between dynein/dynactin and its upstream cortical targeting factors NUMA and LGN (Kiyomitsu and Cheeseman, 2012). Dynein-dynactin movement to the astral microtubule plus ends involves CLIP-170 and LIS1 (Coquelle et al., 2002; Faulkner et al., 2000). In *Drosophila* neuroblasts, dynein and the plus-end motor KHC73/KIF13B act in synergy at microtubule plus ends to promote PINS-mediated spindle positioning (Lu and Prehoda, 2013). However, the microtubule-associated motors mediating dynein-dynactin transport to the astral microtubule plus ends are still unknown. We propose that LGN, NUMA, dynein, and dynactin are recruited to the cell cortex through an astral microtubule- and kinesin 1-dependent transport that is regulated by HTT. How this mechanism is coordinated in space and time with the other pathways remains to be determined.

Finally, the regulation of asymmetric/symmetric divisions is essential for the maintenance of stem cell populations, and it may also be key during tumorigenesis (Cicalese et al., 2009; Driessens et al., 2012; Quyn et al., 2010). In mammary tumoral tissues, symmetric divisions of cancer stem cells may contribute to tumor growth (Cicalese et al., 2009). Thus, our results not only open new lines of investigation for unraveling the mechanisms controlling stem cell self-renewal and cell fate specification in the mammary gland but may also have broader implications for the role of cell divisions in cancer biology.

(J) Model for HTT-mediated regulation of mitotic spindle orientation. During mitosis, HTT is targeted to the spindle poles through its interaction with dynein and promotes the accumulation of NUMA and LGN (1). HTT regulates the kinesin 1-dependent trafficking of dynein, dynactin, NUMA, and LGN along astral microtubules to the cell cortex (2). Once at the cell cortex, the dynein/dynactin/NUMA/LGN complex generates pulling forces on astral microtubules for mitotic spindle positioning (3).
Scale bars, 10 μm. Error bars, SEM. **p < 0.01; ***p < 0.001. See also Figure S6.

EXPERIMENTAL PROCEDURES

Constructs, siRNAs, and Antibodies

A full description of constructs, siRNAs, antibodies, and cell lines is available in Supplemental Experimental Procedures.

Immunostaining

To analyze HTT localization during mitosis, cells were prelysed 30 s in prewarmed 0.5% Triton X-100-PHEM buffer before fixation in anhydrous methanol at −20°C for 3 min and incubation with anti-HTT and anti-γ-tubulin antibodies. Alternatively, cells were fixed in anhydrous methanol at −20°C containing 2% paraformaldehyde (2 min). To visualize P150^{Glued}, dynein, NUMA, and LGN at spindle poles and cell cortex, cells were fixed with 10% trichloracetic acid (7 min), then in cold methanol (−20°C for 10 min). Cells were immunostained with the various antibodies at 4°C (16 hr).

Pictures were captured with a 3D deconvolution imaging system or with a Leica SP5 laser-scanning confocal microscope. Images were treated with ImageJ (http://rsb.info.nih.gov/ij/; NIH).

Spindle Orientation, Quantification, and Image Analyses

Quantification of HTT, HTTFL, or HTTΔYN at spindle poles was achieved using a 3D object counter plug-in (Bolte and Cordelières, 2006). The Line Scan function of ImageJ was used to reveal the relative fluorescence intensity of NUMA, P150^{Glued}, dynein, and LGN along a line crossing the spindle poles and the cell cortex. Spindle orientation in MCF-10A metaphase cells was determined as in Godin et al. (2010). Details can be found in Supplemental Experimental Procedures.

Live-Cell Microscopy

Imaging was performed at 37°C in 5% CO_2 using an inverted microscope (Eclipse T*i*; Nikon) coupled to a spinning-disk confocal system (CSU-X1; Yokogawa). Exposure times and laser power details can be found in Supplemental Experimental Procedures.

Mouse Strains

Mice were bred in a 129SV/C57BL6 genetic background. *Htt*$^{flox/flox}$ mice were used as controls and K5*Cre*;*Htt*$^{flox/flox}$ as mutants. All experiments were performed in accordance with the recommendations of the European Community (86/609/EEC) and the French National Committee (87/848) for the care and use of laboratory animals (permissions 91-448 to S.H. and 76-102 to S.E.).

Histological Analysis

Detailed information for whole-mount preparation and Carmine/X-gal staining, mammary gland processing, and immunostaining can be found in Supplemental Experimental Procedures.

Isolation of Mammary Epithelial Cells and Flow Cytometry

Mammary epithelial cells isolated from the inguinal glands of five 12-week-old virgin K5*Cre* mice were pooled and stained with anti-CD24-FITC, anti-CD49F-PE, anti-CD45-APC, and anti-CD31-APC antibodies (Taddei et al., 2008). CD24-low/CD49F-high (basal) and CD24-high/CD49F-low (luminal) cells were purified using FACSAria III (SORP; Becton Dickinson). CD45- and CD31-positive stromal cells were excluded from the analysis. Conjugated isotype-matching immunoglobulin Gs (IgGs) were used as negative controls. To separate luminal subpopulations, cells were stained with anti-CD49B-APC and anti-SCA1-PE-Cy7 antibodies, and the SCA1$^+$/CD49B$^-$, SCA1$^+$/CD49B$^+$, and SCA1$^-$/CD49B$^+$ were purified (Shehata et al., 2012).

Quantitative RT-PCR

RNA samples were retrotranscribed using the First Strand cDNA Synthesis Kit (Invitrogen). cDNAs were submitted to RT-PCR with the 7900HT Fast Real-Time PCR System using power SYBR Green PCR Master Mix (Applied Biosystems) with the oligonucleotide pairs detailed in Supplemental Experimental Procedures. Fold changes were calculated using the ddCT method. Values were normalized to those for *hprt* and *β-actin*.

Statistical Analyses

GraphPad Prism 6.0 software was used for statistical analysis. Complete statistical analyses with the number of measures are detailed in Supplemental Experimental Procedures.

SUPPLEMENTAL INFORMATION

Supplemental Information includes Supplemental Experimental Procedures, six figures, one table, and six movies and can be found with this article online at http://dx.doi.org/10.1016/j.stemcr.2014.02.011.

ACKNOWLEDGMENTS

We acknowledge F. Saudou for support; I. Cheeseman, Y. Fengwei, M.A. Glukhova, A. Hyman, F. Mechta-Grigoriou, and M. Piel for reagents, mice, and/or discussions; the staff of the Institut Curie imaging, histology, and animal facilities for technical help; and members of the S.H. and Saudou's laboratories for helpful comments. This work was supported by grants from Agence Nationale pour la Recherche-Maladies Rares (ANR-09-BLAN-0080 to S.H. and ANR Blanc 2012-LIVESPIN to X.M.), Association pour la Recherche sur le Cancer (ARC subvention libre n°3188 to S.H. and ARC 2011-LIVESPIN to X.M.), Fondation pour la Recherche Médicale (équipe labellisée to S.H.), INSERM Avenir Grant (R08221JS to X.M.), CNRS (to S.H.), INSERM (to S.H.), and Institut Curie (to S.H.). S.H. is an INSERM investigator.

Received: October 7, 2013
Revised: February 27, 2014
Accepted: February 27, 2014
Published: April 3, 2014

REFERENCES

Asselin-Labat, M.L., Vaillant, F., Sheridan, J.M., Pal, B., Wu, D., Simpson, E.R., Yasuda, H., Smyth, G.K., Martin, T.J., Lindeman, G.J., and Visvader, J.E. (2010). Control of mammary stem cell function by steroid hormone signalling. Nature *465*, 798–802.

Beleut, M., Rajaram, R.D., Caikovski, M., Ayyanan, A., Germano, D., Choi, Y., Schneider, P., and Brisken, C. (2010). Two distinct mechanisms underlie progesterone-induced proliferation in the mammary gland. Proc. Natl. Acad. Sci. USA *107*, 2989–2994.

Bolte, S., and Cordelières, F.P. (2006). A guided tour into subcellular colocalization analysis in light microscopy. J. Microsc. *224*, 213–232.

Bouras, T., Pal, B., Vaillant, F., Harburg, G., Asselin-Labat, M.L., Oakes, S.R., Lindeman, G.J., and Visvader, J.E. (2008). Notch signaling regulates mammary stem cell function and luminal cell-fate commitment. Cell Stem Cell *3*, 429–441.

Caviston, J.P., Ross, J.L., Antony, S.M., Tokito, M., and Holzbaur, E.L. (2007). Huntingtin facilitates dynein/dynactin-mediated vesicle transport. Proc. Natl. Acad. Sci. USA *104*, 10045–10050.

Cicalese, A., Bonizzi, G., Pasi, C.E., Faretta, M., Ronzoni, S., Giulini, B., Brisken, C., Minucci, S., Di Fiore, P.P., and Pelicci, P.G. (2009). The tumor suppressor p53 regulates polarity of self-renewing divisions in mammary stem cells. Cell *138*, 1083–1095.

Colin, E., Zala, D., Liot, G., Rangone, H., Borrell-Pagès, M., Li, X.J., Saudou, F., and Humbert, S. (2008). Huntingtin phosphorylation acts as a molecular switch for anterograde/retrograde transport in neurons. EMBO J. *27*, 2124–2134.

Coquelle, F.M., Caspi, M., Cordelières, F.P., Dompierre, J.P., Dujardin, D.L., Koifman, C., Martin, P., Hoogenraad, C.C., Akhmanova, A., Galjart, N., et al. (2002). LIS1, CLIP-170's key to the dynein/dynactin pathway. Mol. Cell. Biol. *22*, 3089–3102.

Cotton, M., Benhra, N., and Le Borgne, R. (2013). Numb inhibits the recycling of Sanpodo in *Drosophila* sensory organ precursor. Curr. Biol. *23*, 581–587.

Couturier, L., Mazouni, K., and Schweisguth, F. (2013). Numb localizes at endosomes and controls the endosomal sorting of notch after asymmetric division in *Drosophila*. Curr. Biol. *23*, 588–593.

Dompierre, J.P., Godin, J.D., Charrin, B.C., Cordelières, F.P., King, S.J., Humbert, S., and Saudou, F. (2007). Histone deacetylase 6 inhibition compensates for the transport deficit in Huntington's disease by increasing tubulin acetylation. J. Neurosci. *27*, 3571–3583.

Dragatsis, I., Levine, M.S., and Zeitlin, S. (2000). Inactivation of Hdh in the brain and testis results in progressive neurodegeneration and sterility in mice. Nat. Genet. *26*, 300–306.

Driessens, G., Beck, B., Caauwe, A., Simons, B.D., and Blanpain, C. (2012). Defining the mode of tumour growth by clonal analysis. Nature *488*, 527–530.

Faulkner, N.E., Dujardin, D.L., Tai, C.Y., Vaughan, K.T., O'Connell, C.B., Wang, Y., and Vallee, R.B. (2000). A role for the lissencephaly gene LIS1 in mitosis and cytoplasmic dynein function. Nat. Cell Biol. *2*, 784–791.

Gauthier, L.R., Charrin, B.C., Borrell-Pagès, M., Dompierre, J.P., Rangone, H., Cordelières, F.P., De Mey, J., MacDonald, M.E., Lessmann, V., Humbert, S., and Saudou, F. (2004). Huntingtin controls neurotrophic support and survival of neurons by enhancing BDNF vesicular transport along microtubules. Cell *118*, 127–138.

Gjorevski, N., and Nelson, C.M. (2011). Integrated morphodynamic signalling of the mammary gland. Nat. Rev. Mol. Cell Biol. *12*, 581–593.

Godin, J.D., Colombo, K., Molina-Calavita, M., Keryer, G., Zala, D., Charrin, B.C., Dietrich, P., Volvert, M.L., Guillemot, F., Dragatsis, I., et al. (2010). Huntingtin is required for mitotic spindle orientation and mammalian neurogenesis. Neuron *67*, 392–406.

Grill, S.W., and Hyman, A.A. (2005). Spindle positioning by cortical pulling forces. Dev. Cell *8*, 461–465.

Jahchan, N.S., Wang, D., Bissell, M.J., and Luo, K. (2012). SnoN regulates mammary gland alveologenesis and onset of lactation by promoting prolactin/Stat5 signaling. Development *139*, 3147–3156.

Joshi, P.A., Jackson, H.W., Beristain, A.G., Di Grappa, M.A., Mote, P.A., Clarke, C.L., Stingl, J., Waterhouse, P.D., and Khokha, R. (2010). Progesterone induces adult mammary stem cell expansion. Nature *465*, 803–807.

Kiyomitsu, T., and Cheeseman, I.M. (2012). Chromosome- and spindle-pole-derived signals generate an intrinsic code for spindle position and orientation. Nat. Cell Biol. *14*, 311–317.

Konno, D., Shioi, G., Shitamukai, A., Mori, A., Kiyonari, H., Miyata, T., and Matsuzaki, F. (2008). Neuroepithelial progenitors undergo LGN-dependent planar divisions to maintain self-renewability during mammalian neurogenesis. Nat. Cell Biol. *10*, 93–101.

Kotak, S., Busso, C., and Gönczy, P. (2012). Cortical dynein is critical for proper spindle positioning in human cells. J. Cell Biol. *199*, 97–110.

Lancaster, M.A., and Knoblich, J.A. (2012). Spindle orientation in mammalian cerebral cortical development. Curr. Opin. Neurobiol. *22*, 737–746.

Lu, M.S., and Prehoda, K.E. (2013). A NudE/14-3-3 pathway coordinates dynein and the kinesin Khc73 to position the mitotic spindle. Dev. Cell *26*, 369–380.

McGuire, J.R., Rong, J., Li, S.H., and Li, X.J. (2006). Interaction of Huntingtin-associated protein-1 with kinesin light chain: implications in intracellular trafficking in neurons. J. Biol. Chem. *281*, 3552–3559.

Moreira Sousa, C., McGuire, J.R., Thion, M.S., Gentien, D., de la Grange, P., Tezenas du Montcel, S., Vincent-Salomon, A., Durr, A., and Humbert, S. (2013). The Huntington disease protein accelerates breast tumour development and metastasis through ErbB2/HER2 signalling. EMBO Mol. Med. *5*, 309–325.

Morin, X., and Bellaïche, Y. (2011). Mitotic spindle orientation in asymmetric and symmetric cell divisions during animal development. Dev. Cell *21*, 102–119.

Morin, X., Jaouen, F., and Durbec, P. (2007). Control of planar divisions by the G-protein regulator LGN maintains progenitors in the chick neuroepithelium. Nat. Neurosci. *10*, 1440–1448.

Moumen, M., Chiche, A., Cagnet, S., Petit, V., Raymond, K., Faraldo, M.M., Deugnier, M.A., and Glukhova, M.A. (2011). The mammary myoepithelial cell. Int. J. Dev. Biol. *55*, 763–771.

Pardo, R., Molina-Calavita, M., Poizat, G., Keryer, G., Humbert, S., and Saudou, F. (2010). pARIS-htt: an optimised expression platform to study huntingtin reveals functional domains required for vesicular trafficking. Mol. Brain *3*, 17.

Peyre, E., and Morin, X. (2012). An oblique view on the role of spindle orientation in vertebrate neurogenesis. Dev. Growth Differ. *54*, 287–305.

Peyre, E., Jaouen, F., Saadaoui, M., Haren, L., Merdes, A., Durbec, P., and Morin, X. (2011). A lateral belt of cortical LGN and NuMA guides mitotic spindle movements and planar division in neuroepithelial cells. J. Cell Biol. *193*, 141–154.

Quyn, A.J., Appleton, P.L., Carey, F.A., Steele, R.J., Barker, N., Clevers, H., Ridgway, R.A., Sansom, O.J., and Näthke, I.S. (2010). Spindle orientation bias in gut epithelial stem cell compartments is lost in precancerous tissue. Cell Stem Cell *6*, 175–181.

Ramirez, A., Page, A., Gandarillas, A., Zanet, J., Pibre, S., Vidal, M., Tusell, L., Genesca, A., Whitaker, D.A., Melton, D.W., and Jorcano, J.L. (2004). A keratin K5Cre transgenic line appropriate for tissue-specific or generalized Cre-mediated recombination. Genesis *39*, 52–57.

Regan, J.L., Sourisseau, T., Soady, K., Kendrick, H., McCarthy, A., Tang, C., Brennan, K., Linardopoulos, S., White, D.E., and Smalley, M.J. (2013). Aurora A kinase regulates mammary epithelial cell fate by determining mitotic spindle orientation in a Notch-dependent manner. Cell Rep. *4*, 110–123.

Rios, A.C., Fu, N.Y., Lindeman, G.J., and Visvader, J.E. (2014). In situ identification of bipotent stem cells in the mammary gland. Nature *506*, 322–327.

Shackleton, M., Vaillant, F., Simpson, K.J., Stingl, J., Smyth, G.K., Asselin-Labat, M.L., Wu, L., Lindeman, G.J., and Visvader, J.E. (2006). Generation of a functional mammary gland from a single stem cell. Nature *439*, 84–88.

Shehata, M., Teschendorff, A., Sharp, G., Novcic, N., Russell, A., Avril, S., Prater, M., Eirew, P., Caldas, C., Watson, C.J., and Stingl, J. (2012). Phenotypic and functional characterization of the luminal cell hierarchy of the mammary gland. Breast Cancer Res. *14*, R134.

Shirasaki, D.I., Greiner, E.R., Al-Ramahi, I., Gray, M., Boontheung, P., Geschwind, D.H., Botas, J., Coppola, G., Horvath, S., Loo, J.A., and Yang, X.W. (2012). Network organization of the huntingtin proteomic interactome in mammalian brain. Neuron *75*, 41–57.

Shitamukai, A., and Matsuzaki, F. (2012). Control of asymmetric cell division of mammalian neural progenitors. Dev. Growth Differ. *54*, 277–286.

Silberstein, G.B. (2001). Postnatal mammary gland morphogenesis. Microsc. Res. Tech. *52*, 155–162.

Siller, K.H., and Doe, C.Q. (2009). Spindle orientation during asymmetric cell division. Nat. Cell Biol. *11*, 365–374.

Taddei, I., Deugnier, M.A., Faraldo, M.M., Petit, V., Bouvard, D., Medina, D., Fässler, R., Thiery, J.P., and Glukhova, M.A. (2008). Beta1 integrin deletion from the basal compartment of the mammary epithelium affects stem cells. Nat. Cell Biol. *10*, 716–722.

Velier, J., Kim, M., Schwarz, C., Kim, T.W., Sapp, E., Chase, K., Aronin, N., and DiFiglia, M. (1998). Wild-type and mutant huntingtins function in vesicle trafficking in the secretory and endocytic pathways. Exp. Neurol. *152*, 34–40.

Visvader, J.E., and Lindeman, G.J. (2011). The unmasking of novel unipotent stem cells in the mammary gland. EMBO J. *30*, 4858–4859.

Williams, S.E., Beronja, S., Pasolli, H.A., and Fuchs, E. (2011). Asymmetric cell divisions promote Notch-dependent epidermal differentiation. Nature *470*, 353–358.

Woodard, G.E., Huang, N.N., Cho, H., Miki, T., Tall, G.G., and Kehrl, J.H. (2010). Ric-8A and Gi alpha recruit LGN, NuMA, and dynein to the cell cortex to help orient the mitotic spindle. Mol. Cell. Biol. *30*, 3519–3530.

Yalcin-Ozuysal, O., Fiche, M., Guitierrez, M., Wagner, K.U., Raffoul, W., and Brisken, C. (2010). Antagonistic roles of Notch and p63 in controlling mammary epithelial cell fates. Cell Death Differ. *17*, 1600–1612.

Zheng, Z., Zhu, H., Wan, Q., Liu, J., Xiao, Z., Siderovski, D.P., and Du, Q. (2010). LGN regulates mitotic spindle orientation during epithelial morphogenesis. J. Cell Biol. *189*, 275–288.

Stem Cell Reports, Volume *2*

Supplemental Information

Huntingtin Regulates Mammary Stem Cell Division and Differentiation

Salah Elias, Morgane S. Thion, Hua Yu, Cristovao Marques Sousa, Charlène Lasgi, Xavier Morin, and Sandrine Humbert

Supplemental Inventory

Figures S1 to S6

Figure S1. Related to Figure 1.
Shows the full-gating cascade strategy for isolation of mammary epithelial cell subpopulations and the characterization of *Cre* expression in E18.5 mammary rudiment of K5*Cre*;*Htt*$^{flox/flox}$;*R26* embryo.

Figure S2. Related to Figure 3.
Shows that HTT is expressed during pregnancy and lactation and influences apoptosis and proliferation.

Figure S3. Related to Figure 4.
Shows that HTT modulates mitotic spindle orientation in a dynein-dependent manner and regulates the dynamics of the mitotic spindle.

Figure S4. Related to Figure 5.
Shows HTT distribution during mitosis using different huntingtin antibodies targeted against distinct regions, and HTT immunoprecipitation using HTT (4C8) antibody.

Figure S5. Related to Figure 6.
Shows that HTT-Dynein interaction mediates the cortical localization of Dynein/Dynactin/NUMA/LGN complex during mitosis.

Figure S6. Related to Figure 7.
Shows that astral microtubules mediate the localization of Dynein/Dynactin/NUMA/LGN complex during mitosis.

Table S1. Related to Figure S1 and S2.
Shows the epithelial markers used in the study.

Supplemental Movie Legends

Movies S1 and S2. Related to Figure S3.
Show mitotic spindle positioning in Control and si-HTT1-transfected cells.

Movies S3 and S4. Related to Figure 6.
Show Dynein spatial distribution in Control and si-HTT1-transfected cells.

Movies S5 and S6. Related to Figure 6.
Show LGN spatial distribution in Control and si-HTT1-transfected cells.

Extended Experimental Procedures

Statistical Analyses

Supplemental References

Supplemental Figures

Figure S1

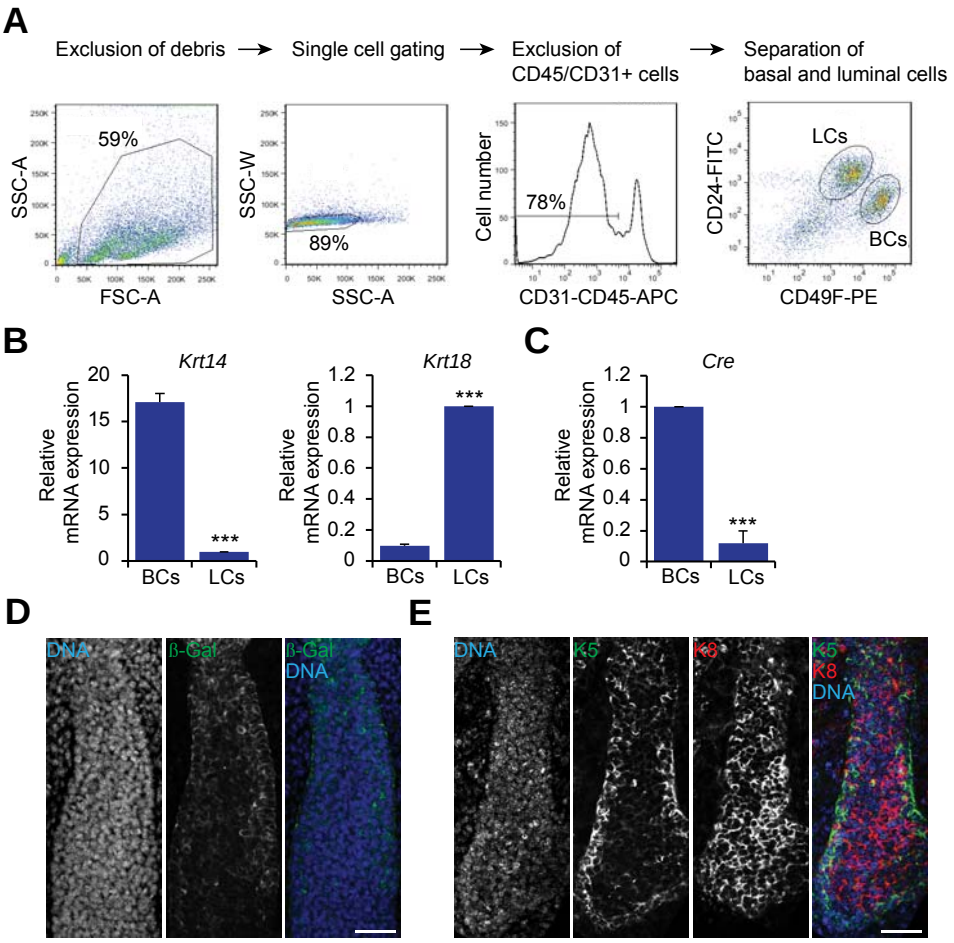

Figure S1. Related to Figure 1

(A) Gating cascade. Samples were gated on forward and side scatter (FSC/SSC) to exclude debris and single cells were isolated using time-of-flight analysis on both FSC and SSC. $CD45^+$ leukocytes and $CD31^+$ endothelial cells were removed and the total epithelial cells were gated on a CD24/CD49F plot. Epithelial subpopulations were isolated from the total epithelial cells.

(B) Quantitative real-time reverse-transcription PCR (RT-qPCR) analysis of *Krt14* and *Krt18* in basal and luminal cell populations isolated from 12-week-old virgin control mouse mammary gland. The values were normalized to *hprt* and *β-actin*.

(C) RT-qPCR analysis of *Cre* in basal and luminal cell populations isolated from 12-week-old virgin mutant mouse mammary gland. The values were normalized to *hprt* and *β-actin*.

(D) Mammary rudiment from an E18.5 female K5*Cre*;*Htt*$^{flox/flox}$;*R26* embryo stained for β-galactosidase (green) and counterstained with DAPI (DNA).

(E) Mammary rudiment from an E18.5 female K5*Cre*;*Htt*$^{flox/flox}$;*R26* embryo stained for keratin 5 (K5, green) and keratin 8 (K8, red) and counterstained with DAPI (DNA).

All scale bars, 50 μm. Error bars, SEM. *** $p<0.001$.

Figure S2

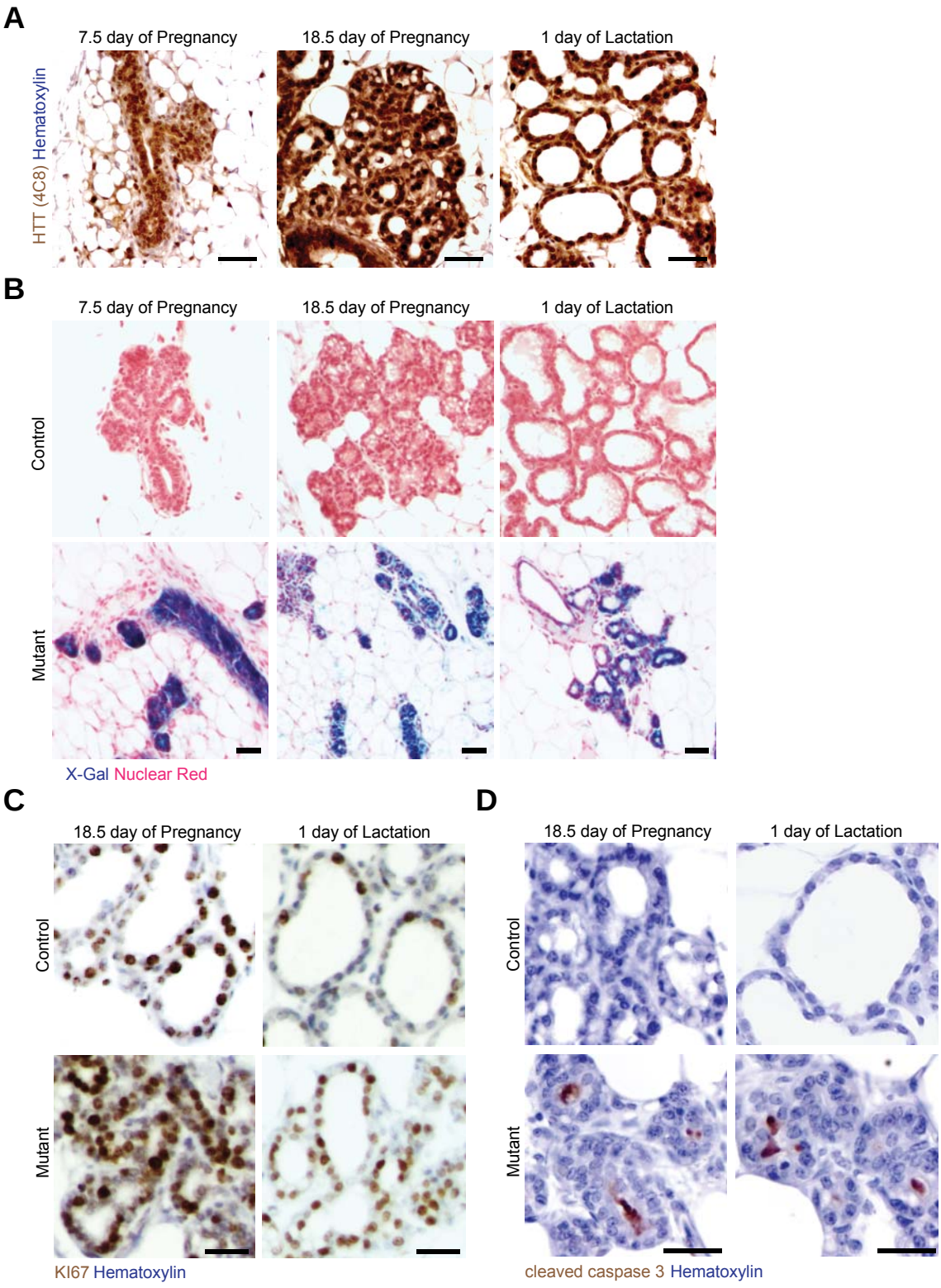
A
7.5 day of Pregnancy
18.5 day of Pregnancy
1 day of Lactation
HTT (4C8) Hematoxylin
B
7.5 day of Pregnancy
18.5 day of Pregnancy
1 day of Lactation
Control
Mutant
X-Gal Nuclear Red
C
18.5 day of Pregnancy
1 day of Lactation
Control
Mutant
KI67 Hematoxylin
D
18.5 day of Pregnancy
1 day of Lactation
Control
Mutant
cleaved caspase 3 Hematoxylin

Figure S2. Related to Figure 3

(A) Mammary gland sections from 7.5 and 18.5 day pregnant and 1 day lactating non-transgenic C57Bl6/J mice stained for HTT.

(B) Sections from *Lac-Z*-stained mammary glands derived from 7.5 and 18.5 day pregnant and 1 day lactating control and mutant K5*Cre*;*Htt*$^{flox/flox}$;*R26*.

(C) Mammary gland sections from 18.5 day pregnant and 1 day lactating control and mutant mice stained for cleaved caspase 3.

(D) Mammary gland sections from 18.5 day pregnant and 1 day lactating control and mutant mice stained for KI67.

All scale bars, 50 μm.

Figure S3

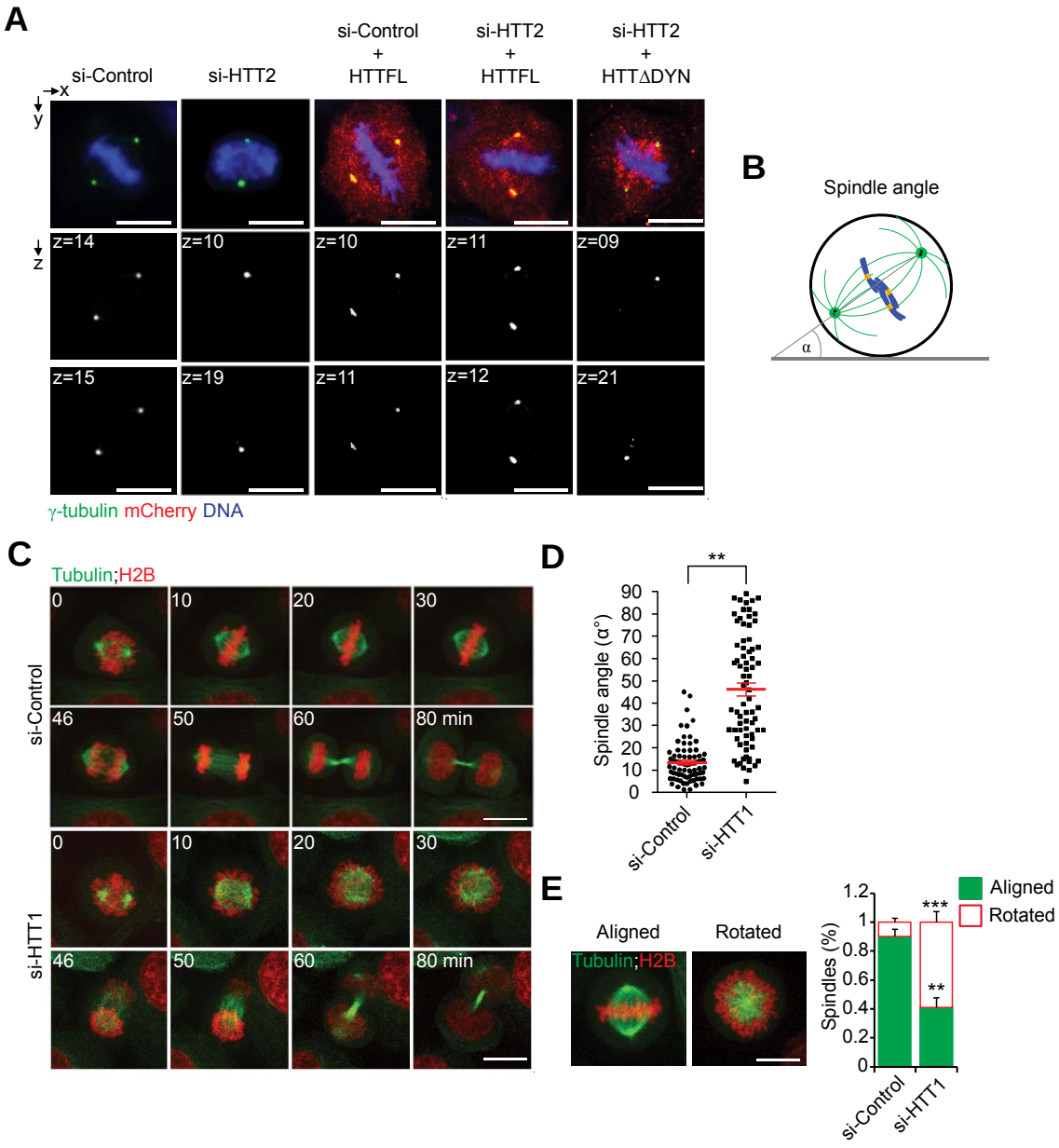

Figure S3. Related to Figure 4

(A) Mammary cells transfected with si-Control + HTTFL, si-HTT2 + HTTFL or si-HTT2 + HTTΔDYN stained for γ-tubulin (green) and HTT (mCherry, red) and counterstained with DAPI (DNA).

(B) Schemes illustrating measurement of spindle angle α in mitotic mammary cells.

(C) HeLa cells stably expressing GFP-tubulin and H2B-mCherry were transfected with si-Control or si-HTT1 RNAs and video-recorded every 2 min for 2 hr, as the cells progressed through mitosis. Image stacks of 32 planes spaced 0.6 μm apart were taken at 6 stage positions every 2 min for 2 h. Maximum intensity projections of tubulin and histone H2B are shown at the times indicated in the figure. See also Movies S1 and S2.

(D) Distribution and mean spindle angle in metaphase HeLa cells stably expressing GFP-tubulin and H2B-mCherry cells and treated with si-Control or si-HTT1 RNAs.

(E) Left: Maximum intensity projections of tubulin and histone H2B from HeLa cells stably expressing GFP-tubulin and H2B-mCherry, indicating aligned and rotated mitotic spindle during metaphase. Right: Percentage of si-Control and si-HTT1 RNA-transfected Hela cells with aligned or rotated mitotic spindle.

All scale bars, 10 μm. Error bars, SEM. ** $p<0.01$; *** $p<0.001$.

Figure S4

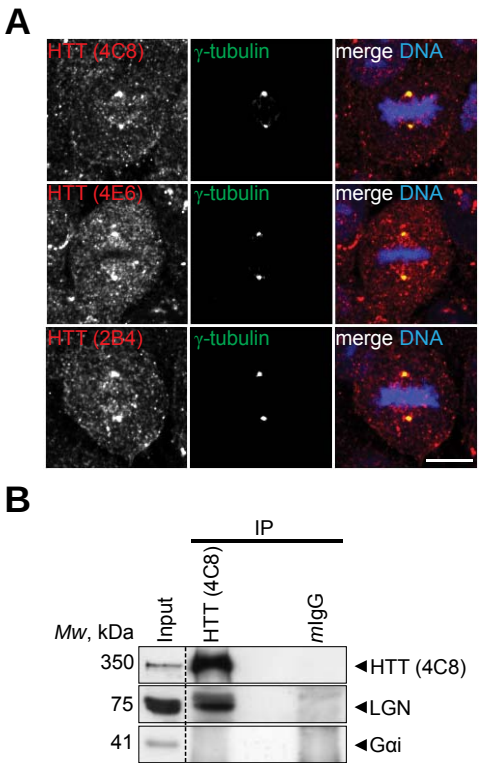

Figure S4. Related to Figure 5

(A) Mammary cells stained for γ-tubulin and HTT (4C8, 4E6 and 2B4 antibodies) and counterstained with DAPI (DNA). Scale bars, 10 µm.

(B) HTT, LGN and $G_{\alpha i}$ were immunoprecipitated using HTT (4C8) antibody from mammary cells arrested in metaphase before cell lysis. Mouse IgG (*m*IgG) was used as a negative control. The immunoprecipitates were analyzed by immunoblotting with anti-HTT (4C8), anti-LGN and anti-$G_{\alpha i}$ antibodies.

Figure S5

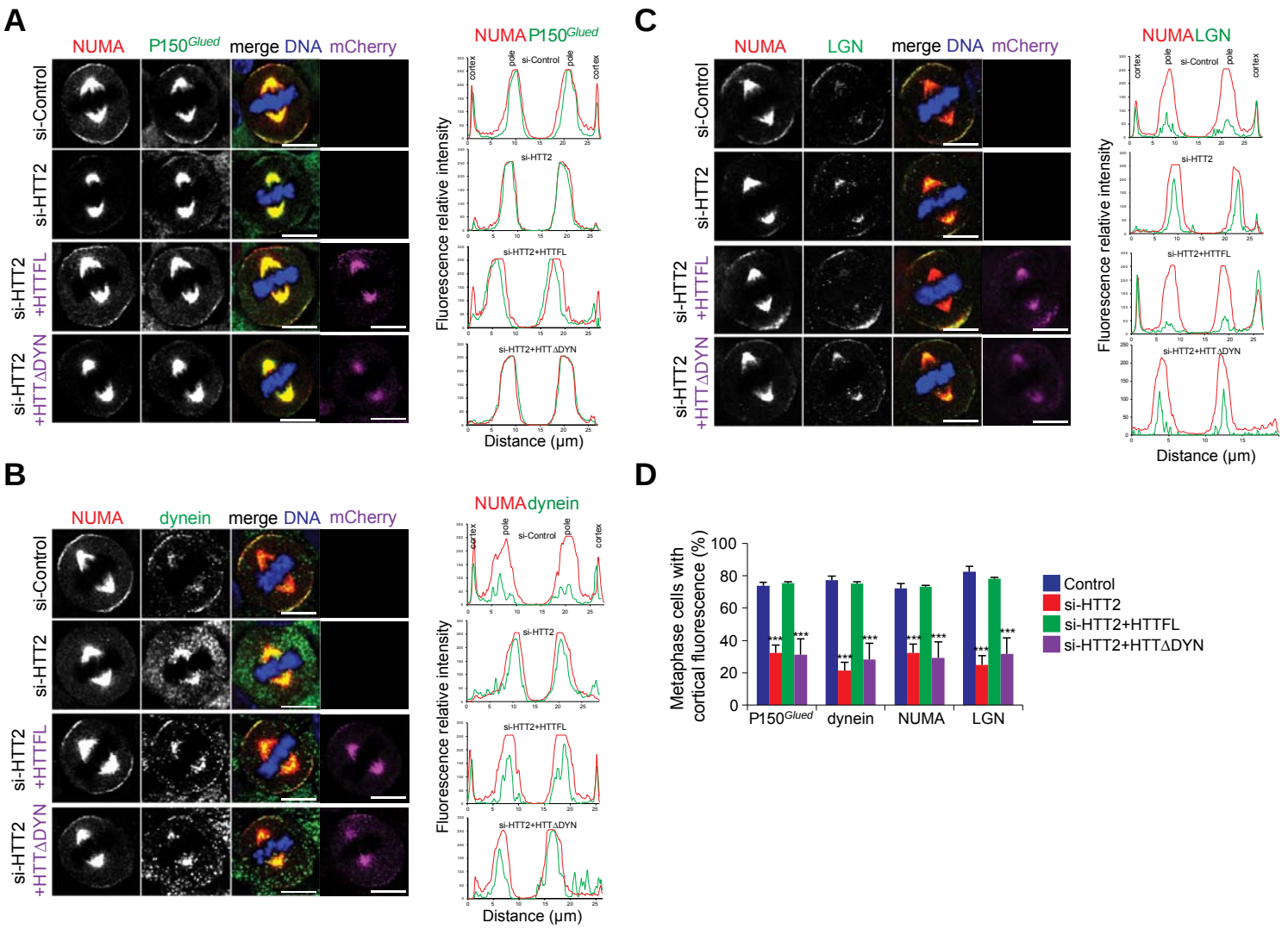

Figure S5. Related to Figure 6

(A to C) Mammary cells transfected with si-Control, si-HTT2, si-Control + HTTFL, si-HTT2 + HTTFL or si-HTT2 + HTTΔDYN and stained for NUMA and P150^{Glued} (A), dynein (B) or LGN (C) and counterstained with DAPI (DNA). Right: line scan analysis (relative fluorescence intensity) showing the spatial distribution of NUMA and P150^{Glued} (A), dynein (B) or LGN (C).

(D) Percentage of mammary cells transfected showing cortical P150^{Glued}, dynein, NUMA and LGN at metaphase.

All scale bars, 10 µm. Error bars, SEM. *** p<0.001.

Figure S6

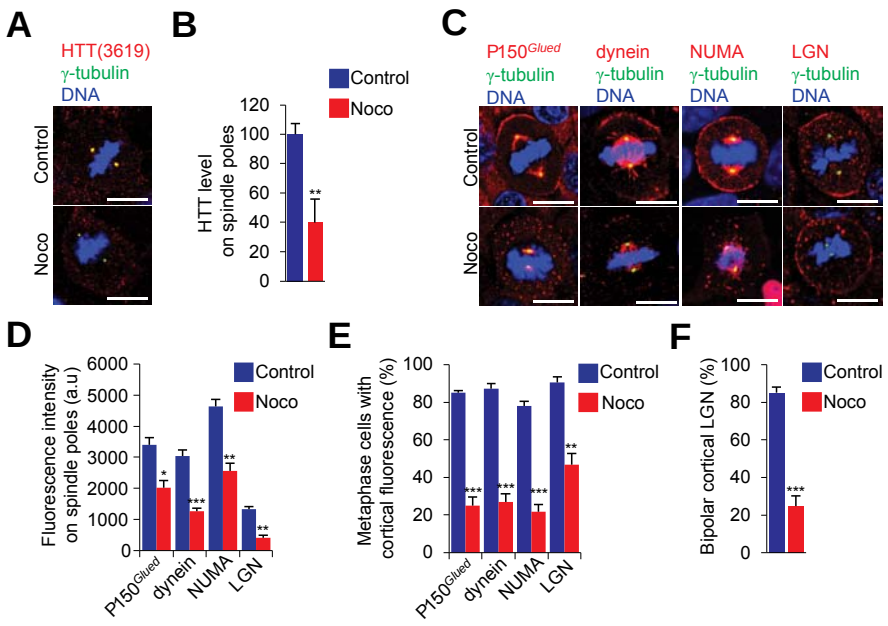

Figure S6. Related to Figure 7

(A) Mammary cells treated with DMSO (Control) or 40 nM nocodazole (Noco) for 20 min and stained for HTT and γ-tubulin and counterstained with DAPI (DNA).

(B) HTT abundance at spindle poles in Control and Noco metaphase cells.

(C) Control and Noco mammary cells stained for γ-tubulin with P150^{Glued}, dynein, NUMA or LGN and counterstained with DAPI (DNA).

(D) P150^{Glued}, dynein, NUMA and LGN abundance at spindle poles in Control and Noco mammary metaphase cells.

(E) Percentage of Control and Noco mammary cells with cortical accumulation of P150^{Glued}, dynein, NUMA and LGN at metaphase.

(F) Percentage of LGN-positive Control and Noco mammary cells with bipolar cortical LGN labelling as opposed to homogeneous labelling throughout the cell cortex.

All scale bars, 10 µm. Error bars, SEM. * $p<0.005$; ** $p<0.01$; *** $p<0.001$.

Table S1. Epithelial Markers Used

Epithelial compartment	Gene	Protein	Method
Basal	*Trp63*	P63	RT-qPCR
	Krt14	Keratin 14 (K14)	RT-qPCR, IHC
	Krt5	Keratin 5 (K5)	IHC
	Cd24	Heat stable antigen (HSA or CD24), *low expression*	FACS
	Itgb1	β1 integrin (CD29), *high expression*	IHC
	Itga6	α6 integrin (CD49F), *high expression*	FACS
	Snai1	Snail 1	RT-qPCR
	Snai2	Snail 2	RT-qPCR
	Vim	Vimentin	RT-qPCR
Luminal	*Gata3*	GATA3	RT-qPCR
	Cdh1	E-cadherin	IHC
	Krt8/18	Keratin 8/18 (K8/18)	RT-qPCR, IHC
	Cd24	Heat stable antigen (HSA or CD24), *high expression*	FACS
	Itgb1	β1 integrin (CD29), *low expression*	IHC
	Itga6	α6 integrin (CD49F), *low expression*	FACS
	Itga2	α2 integrin (CD49B), *luminal progenitors*	FACS
	Elf5	E74-like factor 5 (ELF5), *luminal progenitors*	RT-qPCR
	Kit	proto-oncogene KIT, *luminal progenitors*	RT-qPCR
	Sca1	Stem cell antigen 1 (SCA1), *mature luminal cells*	FACS
	Esr1	Estrogen receptor 1 (ER1), *mature luminal cells*	RT-qPCR, IHC
	Pgr	Progesterone receptor (PR), *mature luminal cells*	RT-qPCR
	Prlr	Prolactin Receptor (PRLR), *mature luminal cells*	RT-qPCR

Supplemental Movie Legends

Movie S1. Mitotic Spindle Positioning in Control Cells, Related to Figure S3C

HeLa cells stably expressing GFP-tubulin and mCherry-histone H2B were transfected with si-Control RNA for 72 h. Images corresponding to 32 planes spaced by 0.6 μm through the cell volume were collected every 2 min, as the cells progressed through mitosis using a spinning-disk confocal microscope (CSU-X1; Yookogawa). Maximum intensity projections of tubulin (green) and histone H2B (red) are shown through time; each frame corresponds to 2 min.

Movie S2. Loss of Huntingtin Alters Mitotic Spindle Orientation, Related to Figure S3C

HeLa cells stably expressing GFP-tubulin and mCherry-histone H2B were transfected with si-HTT1 RNA for 72 h. Images corresponding to 32 planes spaced by 0.6 μm through the cell volume were collected every 2 min, as the cells progressed through mitosis using a spinning-disk confocal microscope (CSU-X1; Yookogawa). Maximum intensity projections of tubulin (green) and histone H2B (red) are shown through time; each frame corresponds to 2 min.

Movie S3. Dynein Spatial Distribution in Control Cells, Related to Figure 6F

HeLa cells stably expressing DHC-GFP were transfected with si-HTT1 RNA for 72 h. Images corresponding to 35 planes spaced by 0.6 μm through the cell volume were collected every 3 min, as the cells progressed through mitosis using a spinning-disk confocal microscope (CSU-X1; Yookogawa). Maximum intensity projections of DHC are shown through time; each frame corresponds to 3 min.

Movie S4. Loss of Huntingtin Alters the Dynamics of Dynein, Related to Figure 6F

HeLa cells stably expressing DHC-GFP were transfected with si-HTT1 RNA for 72 h. Images corresponding to 35 planes spaced by 0.6 μm through the cell volume were collected every 3 min, as the cells progressed through mitosis using a spinning-disk confocal microscope (CSU-X1; Yookogawa). Maximum intensity projections of DHC are shown through time; each frame corresponds to 3 min.

Movie S5. LGN Spatial Distribution in Control Cells, Related to Figure 6F

HeLa cells stably expressing GFP-LGN were transfected with si-HTT1 RNA for 72 h. Images corresponding to 35 planes spaced by 0.6 μm through the cell volume were collected every 3 min, as the cells progressed through mitosis using a spinning-disk confocal microscope (CSU-X1; Yookogawa). Maximum intensity projections of LGN are shown through time; each frame corresponds to 3 min.

Movie S6. Loss of Huntingtin Alters the Dynamics of LGN, Related to Figure 6F

HeLa cells stably expressing GFP-LGN were transfected with si-HTT1 RNA for 72 h. Images corresponding to 35 planes spaced by 0.6 μm through the cell volume were collected every 3 min, as the cells progressed through mitosis using a spinning-disk confocal microscope (CSU-X1; Yookogawa). Maximum intensity projections of LGN are shown through time; each frame corresponds to 3 min.

Extended Experimental Procedures

Constructs and siRNAs

pARIS-mCherry-HTT and pARIS-mCherry-HTTΔdynein (referred to herein as HTTFL and HTTΔDYN, respectively) were previously described (Pardo et al., 2010). The RNA oligonucleotides for siRNA (Eurogentec) were annealed and used at 8 μM in MCF-10A and HeLa cells. The following pairs of oligonucleotides were used: Huhtt4487-sens (5'-GCAGGUUUUAGAUUUGCUG-3') and Huhtt4487-antisens (5'-CAGCAAAUCUAAAACCUGC-3') for siRNA against human HTT (si-HTT1); Huhtt585-sens (5'-AACUUUCAGCUACCAAGAAAG-3') and Huhtt585-antisens (5'-CUUUCUUGGUAGCUGAAAGUU-3') for siRNA against human HTT (si-HTT2) and si-dynein-sens (5'-GCAAUGCAGUGGCUCCUUU-3'), si-dynein-antisens (5'-AAAGGAGCCACUGCAUUGC-3') for siRNA against mouse/rat/human heavy chain of dynein (si-dynein) and si-kinesin-1-sens (5'-GCAGUCAGGUCAAAGAAUA-3') and si-kinesin-1-antisens (5'-UAUUCUUUGACCUGACUGC-3') for siRNA against mouse/rat/human KIF5B (si-kinesin-1). siRNA negative control (si-Control) from Eurogentec (OR-0030-neg05) was used. The HTT siRNAs were extensively used to target HTT function in dynein/dynactin dependent transport along microtubules in cells without off-target effects, as shown in rescue experiments and by the use of other siRNAs (Colin et al., 2008).

Cell lines and Transfection

MCF-10A, a spontaneously immortalized nontransformed human mammary epithelial cell line derived from the breast tissue (Soule et al., 1990) was maintained in DMEM/F12 (Invitrogen, Carlsbad, CA) supplemented with 5% donor horse serum, 20 ng/ml EGF (Peprotech, Rocky Hill,

NJ), 10 μg/ml insulin (Sigma, St Louis, MO), 1 ng/ml cholera toxin (Sigma), 100 μg/ml hydrocortisone (Sigma), 50 U/ml penicillin, and 50 μg/ml streptomycin (Invitrogen). Cells were spread in 10 cm^2 plate and in glass coverslips for immunoblotting and immunofluorescence experiments respectively, and transfected using Lipofectamin2000 (Invitrogen) with si-Control or si-HTT1/2 or si-dynein. For rescue experiments, expression of HTTFL and HTTΔDYN was achieved by co-electroporation of the HTTFL and HTTΔDYN constructs with si-Control or si-HTT2. After 48-72 hr, cells were lysed or fixed and immunoprocessed.

HeLa cells stably expressing GFP-tubulin (green) and H2B-mCherry (red) or DHC-GFP or GFP-LGN were cultured as previously described (Steigemann et al., 2009), plated on glass coverslips and transfected using Lipofectamin2000 with si-control or si-HTT1/2. After 72 hr, transfected cells were analyzed by spinning disk confocal videomicroscopy.

Drug Treatment

Drugs were dissolved in DMSO and kept at -20°C as 10 mM stock solutions. To enrich MCF-10A cells in metaphase, cells were seeded in 10 cm dishes (3 x 10^6 cells per dish) 24 h before treatment with 9 μM RO-3306 (Roche) for 18 hr allowing CDK1 inhibition (Vassilev et al., 2006). Cells were released from the G_2 block by washing three times in prewarmed drug-free media and incubated in fresh media for 35 min to enrich in metaphase cells. ~50% of cells were in metaphase (data not shown). To depolymerize astral microtubules, MCF-10A cells were treated with 40 nM nocodazole (Sigma) for 20 min.

Antibodies and Immunostaining Procedures

Anti-HTT antibodies used in this study were previously described: mAb 2B4 (epitope 49-64, clone HU 2B4, Euromedex) (Lunkes et al., 2002), mAb 4C8 (epitope 445-456, clone HU-4C8-

As, Euromedex), mAb 4E6 (epitope 1247-1646, clone HU-4E6, Millipore), pAb, SE3619 (Godin et al., 2010).

For immunofluorescence, the primary monoclonal antibodies used were: anti-α-tubulin DM1A (1:1000; Sigma), anti-NUMA (1:200; Calbiochem), anti-HTT 4C8 (1:500), anti-P150^{Glued} (1:100; BD Bioscience), anti-intermediary chain 74.1 of mammalian cytoplasmic dynein (1:200; Chemicon), anti-γ-tubulin GTU88 (1:300; Sigma) and anti-heavy chain KIF5A/B of mammalian cytoplasmic kinesin-1 (1:200; Covance). The primary polyclonal antibodies used were: anti-HTT SE3619 (1:100), anti-NUMA (1:200; Novus Biologicals), anti-LGN (Kaushik et al., 2003) and anti-γ-tubulin AT15 (1:500; Sigma). Secondary antibodies used were goat anti-mouse and anti-rabbit conjugated to AlexaFluor-488 or AlexaFluor-555 (Molecular Probes) at 1:200. Cells were grown on glass coverslip transfected with various constructs or siRNA.

To analyze HTT localization during mitosis, cells were prelysed 30 sec in prewarmed 0.5% Triton X-100-PHEM buffer before being fixed in anhydrous methanol at -20°C for 3 min and incubated with anti-HTT 4C8, anti-HTT 2B4, anti-HTT 4E6 or anti-HTT SE3619 and γ-tubulin. Alternatively, cells were fixed in anhydrous methanol at -20°C, containing 2% paraformaldehyde for 2 min and incubated with anti-HTT 4C8 or anti-HTT SE3619 and anti-P150^{Glued}, anti-dynein, anti-NUMA or anti-LGN overnight at 4°C.

P150^{Glued}, dynein, NUMA and LGN at spindle poles and the cell cortex were visualized as follow: cells were first fixed with 10% trichloacetic acid for 7 min. Then cells were fixed for 10 min in cold methanol (-20°C) and washed 3 times before immunostaining. Cells were double immunostained with anti-NUMA and anti-P150^{Glued} or anti-dynein or anti-LGN antibodies overnight at 4°C and then with anti-mouse and anti-rabbit AlexaFluor-488 or AlexaFluor-555.

For all immunostainings, the slides were counterstained with DAPI (Roche) and mounted in Mowiol. The pictures were captured either with a three-dimensional deconvolution imaging system or with a Leica SP5 laser scanning confocal microscope equipped with a X63 oil-immersion objective. *Z*-stack steps were of 0.2 μm. Images were treated with ImageJ (http://rsb.info.nih.gov/ij/, NIH, USA).

Spindle Orientation Quantification and Image Analyses

For quantification of HTT, HTTFL, HTTΔYN, P150^{Glued}, NUMA, LGN or kinesin-1 at spindle poles, cells were stained for the protein of interest and γ-tubulin. Quantification was achieved using 3D object counter plug-in (Bolte and Cordelieres, 2006); available at http://imagejdocu.tudor.lu/doku.php?id=plugin:analysis:3d_object_counter:start. Total volume and intensity of the particles were retrieved for further analysis.

To measure the relative fluorescence intensity of NUMA, P150^{Glued}, dynein and LGN, at spindle poles and the cell cortex, a 30-pixel line was drawn across the spindle poles and the opposing cell borders using ImageJ software. The Line Scan function of ImageJ was used to reveal the relative fluorescence intensity across the line.

Spindle orientation in MCF-10A metaphase cells was quantified using ImageJ software (http://rsb.info.nih.gov/ij/, NIH, USA). A line crossing both spindle poles was drawn on the *Z* projection pictures and repositioned along the *Z*-axis using the stack of *Z*-sections. The angle between the pole-pole and the substratum plane was calculated by an ImageJ Plug-in (Godin et al., 2010). Spindle lengths and cell lengths were quantified along the line that crosses both spindle poles.

Live-Cell Microscopy

For live-cell imaging, cells were plated in 24 mm coverglass, mounted in 6-well plate (TPP). Imaging was performed at 37°C in 5% CO_2 using an inverted microscope (Eclipse T*i*; Nikon) with a 60 x 1.42 NA oil immersion objective coupled to a spinning-disk confocal system (CSU-X1; Yookogawa) fitted with an EM-CCD camera (Evolve; Photometrics). Exposure times were 50 msec for GFP-tubulin or mCherry-tagged histone H2B and 10% laser power, 200 msec and 8% laser power for GFP-LGN, and 200 msec and 15% laser power for DHC-GFP. For Figure 5G, image stacks of 32 planes spaced 0.6 μm apart were taken at 6 stage positions every 2 min for 2 h. For Figure 7F, 35 planes spaced 0.6 μm apart were captured at 10 stage positions every 3 min for 2 h. Maximum intensity projection of the fluorescent channels was performed. Images were treated with ImageJ.

Cell Extracts, Immunoblotting and Immunoprecipitation Experiments

MCF-10A and Hela cells were lysed in NP40 buffer (50 mM Tris, pH 7.4, 250 mM NaCl, 5 mM EDTA, 50 mM NaF, 1 mM Na3VO4, 1% Nonidet P40 (NP40), 0.02% NaN_3), containing protease inhibitor cocktail (Sigma), and centrifuged at 11,000 x g for 10 min at 4°C. Proteins (20-30 μg) were loaded onto SDS-PAGE (polyacrylamide gel electrophoresis) and subjected to Western blot analysis. Primary monoclonal antibodies used were: anti-HTT 4C8 (1:3000), anti-P150^{Glued} (1:1000), anti-α-tubulin (1:5000), anti-dynein (1:1000) and anti-kinesin-1 (1:1000). Primary polyclonal antibodies used were: anti-NUMA (1:1000), anti-LGN (1:500), anti-$G_{\alpha i1}$ (1:1000; Santa Cruz Biotechnology) and anti-mCherry (1:1000; Institut Curie, Paris). Secondary HRP-conjugated goat anti-mouse/anti-rabbit antibodies (Amersham) at 1:10 000 were used.

For immunoprecipitations, metaphase MCF-10A cells were lysed in IP buffer (Tris 50 mM, pH 7.4, 250 mM NaCl, 5 mM EDTA, 50 mM NaF, 1% Na_3VO_4, 1% NP40, 0.02% NaN_3, 50mM KH_2PO_4) containing protease inhibitor cocktail. Lysates (500 µg at 1 µg/µl) were precleared 1 h at 4°C with 50 µl of a 50% solution of protein A or G beads. Extracts were incubated for 1 h at 4°C with 5 µg of anti-HTT (4C8) antibody or anti-dynein or anti-IgG prebound with 50 µl of a 50% solution of protein A or G sepharose beads (Sigma). Beads were washed three times with IP buffer. Bound proteins were eluted with SDS loading buffer and resolved by SDS-PAGE and subjected to immunoblotting analysis.

Mouse Strains

Transgenic mice expressing the Rosa26LacZ reporter strain, carrying a loxP-stop loxP-lacZ cassette, and the Cre recombinase under the control of the K5 promoter (K5*Cre*) were provided by P. Soriano and J. Jorcano (Ramirez et al., 2004; Soriano, 1999). The generation of $Htt^{flox/flox}$ mice was previously described (Dragatsis et al., 2000). All mice were bred in a 129SV/C57BL6 genetic background. $Htt^{flox/flox}$ mice were used as controls and K5*Cre*;$Htt^{flox/flox}$ as mutants. All experiments were performed in strict accordance with the recommendations of the European Community (86/609/EEC) and the French National Committee (87/848) for care and use of laboratory animals (permissions 91-448 to S.H. and 76-102 to S.E.).

Whole Mounts

Whole mounts were prepared by fixing the glands on glass slides with MethaCarn solution (60% methanol, 30% chloroform, 10% glacial acetic acid) overnight at room temperature. The mounts were hydrated by sequential incubation in ethanol solutions of decreasing concentration: 100%, (overnight), 70%, 50%, and 30% (15 min each), distilled water (2 x 5 min), and stained overnight

with an aqueous solution of 2% carmine (Sigma, Buchs, Switzerland) and 5% aluminum potassium sulphate (Sigma, Buchs, Switzerland). The mounts were dehydrated in ethanol solutions (70%, 90%, 95%, and 2 x 100%, for 15 min each) and cleared with xylene overnight. Images were captured with an Epson Perfection 3200 scanner.

X-Gal Staining

For whole-mount X-Gal staining, mammary glands were fixed in 2.5% paraformaldehyde in PBS, pH 7.5, for 1 hr at 4°C, and stained overnight at 30°C (Biology of the Mammary Gland, http://mammary.nih.gov). For histological analyses, glands were embedded in paraffin, and 7 µm-thick sections were cut, dewaxed and counterstained with Nuclear Fast Red.

Histology and Immunostaining

Dissected mammary fat pads were spread out on a glass slide, fixed in MethaCarn and embedded in paraffin. 7 µm-thick Sections were cut and deparaffinized before staining. Sections were incubated overnight at 4 °C with primary antibodies, followed by incubation for 1 hr at room temperature with secondary antibodies and 3 min with DAPI. Primary antibodies used were: rabbit polyclonal anti-K5 (1:2000; Covance), anti-K14 (1:500; clone AF64, Covance), anti-PAR3 (1:200; Chemicon), anti-aPKC (1:200; clone C-20, Santa Cruz Biotechnology), anti-p-STAT5A (Tyr694, 1:100; Cell Signalling), anti-cleaved caspase 3 (1:100; Cell Signalling), anti-WAP (1:300; clone R-131; Santa Cruz Biotechnology), anti-ERα (1:50; Santa Cruz Biotechnology); rabbit monoclonal anti-KI67 (1:100; clone SP6, Neo Markers); rat monoclonal anti-β1 integrin (1:200; clone MB1.2, Chemicon) and mouse monoclonal anti K8 (1:100; clone Ks 8.7, Progen Biotechnik), anti-α-smooth muscle actin (1:100; clone 1A4, Sigma-Aldrich), anti-α-tubulin

DM1A (1:1000; Sigma), anti-ZO1 (1:50; Invitrogen), anti-E-cadherin (1:200; BD Bioscience). Antigen retrieval was performed by boiling the slides for 10 min in a microwave in 10 mM citrate buffer (pH 6) for cleaved caspase 3, KI67 and p-STAT5A, or in EDTA buffer (pH 8.8) for 10 min for PAR3, aPKC, ZO1 and E-cadherin antibodies. Secondary antibodies used were goat anti-mouse and anti-rabbit conjugated to AlexaFluor-488 or AlexaFluor-555 or Biotin (Vector Laboratories).

Alternatively, frozen 10 to 14 μm-thick sections were cut and air-dried for 30 min, then fixed for 10 min with 4% paraformaldehyde, demasked with acetone at -20°C, for 10 min for γ-tubulin staining, and then blocked for 1 h in BSA/NGS block (3% BSA, 5% NGS, 0.2% Triton X-100 in PBS). Sections were incubated overnight at 4 °C with primary antibodies, followed by incubation for 1 h at room temperature with secondary antibodies and 3 min with DAPI. Primary antibodies used were: rabbit polyclonal anti-NUMA (1:100), anti-LGN (1:100), anti-K5 (1:500); rat monoclonal anti-β1 integrin (1:200; clone MB 1.2, Chemicon); mouse monoclonal anti-HTT (4C8, 1:300), anti-α-tubulin (1:500) and anti-γ-tubulin (1:200). Secondary antibodies used were goat anti-mouse, anti-rat and anti-rabbit conjugated to AlexaFluor-488 or AlexaFluor-555 or AlexaFluor-647 (Vector Laboratories).

Ventral skin of E18 embryos was fixed in 4% paraformaldehyde and immunostained as described elsewhere (Kogata and Howard, 2013). Primary antibodies used were: rabbit polyclonal anti-K5 (1:200; Covance); anti-β-glactosidase (1:100; 5 Prime 3 Prime) and mouse monoclonal anti K8 (1:50; clone Ks 8.7, Progen Biotechnik). Secondary antibodies used were goat anti-mouse and anti-rabbit conjugated to AlexaFluor-488 or AlexaFluor-555 (Vector Laboratories).

Isolation of the Mammary Epithelial Cells and Flow Cytometry

To isolate mammary epithelial cells, mammary fat pads were mechanically dissociated with scissors and scalpel and digested for 90 min at 37 °C in CO2-independent medium (Invitrogen) supplemented with 5% fetal bovine serum, 3 mg/ml collagenase (Roche Diagnostics) and 100 U/ml hyaluronidase (Sigma). Cells were sequentially resuspended in 0.25% trypsin-EDTA for 1 min, and then 5 min in 5 mg/ml dispase (Roche Diagnostics) with 0.1 mg/ml DNase I (Sigma) followed by filtration trough a 40-μm mesh. Red blood cells were lysed in NH_4Cl.

To separate basal and luminal cells, mammary epithelial cells isolated from the inguinal glands of five 12-week-old virgin K5*Cre* mice were pooled, stained with anti-CD24-FITC (clone M1/69; BD Pharmingen), anti-CD49F-PE (clone OXM178; Chemicon), anti-CD45-APC (clone 30-F11; Biolegend) and anti-CD31-APC (clone MEC13.3; Biolegend) antibodies, as described elsewhere (Shackleton et al., 2006; Stingl et al., 2006; Taddei et al., 2008). CD24-low/α6-high (basal) and CD24-high/α6-low (luminal) cells were purified using FACSAria III (SORP) (Becton Dickinson). CD45- and CD31-positive stromal cells were excluded from the flow cytometry analysis. Conjugated isotype-matching IgGs were used as negative controls.

To separate different sub-populations within luminal compartment, sorted luminal cells (pure at 98%) were stained with anti-CD49B-APC (clone HMα2, BD Pharmingen) and anti-SCA1-PE-Cy7 (clone D7, BD Pharmingen) antibodies. The following cell populations were purified: $SCA1^+/CD49B^-$, $SCA1^+/CD49B^+$ and $SCA1^-/CD49B^+$ (Shehata et al., 2012).

Mammary Colony Forming Assay

In vitro Matrigel colony forming assays were performed as described (Stingl et al., 2006). Single mammary cell suspensions were prepared from the inguinal glands and 5,000 BCs or LCs were

seeded in 50 µL Matrigel and cultured in DMEM/F12 medium containing 1% fetal calf serum (FCS), B27. Colonies were scored after 6 days.

Quantitative RT-PCR

RNA samples were retrotranscribed using the First-Strand cDNA Synthesis Kit (Invitrogen). cDNAs were diluted 1:10 and submitted to RT-PCR with 7900HT Fast real time PCR system (Applied biosystems) using power SYBR Green PCR Master mix (Applied biosystems) with the following oligonucleotide pairs: *Htt* (5'-CTCAGAAGTGCAGGCCTTACCT-3', 5'-GATTCCTCCGGTCTTTTGCTT-3' and 5'-CTCAGAAGTGCAGGCCTTACCT-3', 5'-GATTCCTCCGGTCTTTTGCTT-3') (Benn et al., 2008), *Cre* (5'-TTCCCGCAGAACCTGAAGAT-3', 5'- GCCGCATAACCAGTGAAACA-3') (Taddei et al., 2008), *Gata3* (5'- AGCCACATCTCTCCCTTCAG-3', 5'-AGGGCTCTGCCTCTCTAACC-3'), *Dll1* (5'-CATGAACAACCTAGCCAATTGC-3', 5'-GCCCCAATGATGCTAACAGAA-3'), *Dll3* (5'-CCTGAGGTTACAAGACGGTGCT-3', 5'-CAGGCCTCTCGTGCATAAATG-3'), *Jag1* (5'-ACACAGGGATTGCCCACTTC-3', 5'-AGCCAAAGCCATAGTAGTGGTCAT-3'), *Jag2* (5'-CGACTCACACTGCGCTTCA-3', 5'-TCGGATTCCAGAGCAGATAGC-3'), *Notch1* (5'-ACAACAACGAGTGTGAGTCC-3', 5'-ACACGTGGCTCCTGTATATG-3'), *Notch2* (5'-TGACTGTTCCCTCACTATGG-3', 5'-CACGTCTTGCTATTCCTCTG-3'), *Notch3* (5'-AGATCAATGAGTGTGCATCC-3', 5'-GCAGACTCCATGACTACAGG-3'), *Notch4* (5'-GAGGACCTGGTTGAAGAATTGATC-3', 5'-TGCAGTTTTTCCCCTTTTATCC-3'), *Hey1* (5'-TGAGCTGAGAAGGCTGGTAC-3', 5'-ACCCCAAACTCCGATAGTCC-3'), *Hes6* (5'-AAGCTAGAGAACGAAGAGGT-3', 5'-TCAGCTGAGAAGTGGCATC-3') (Bouras et al., 2008), *Krt14* (5'-GCTCTTGTGGTATCGGTGGT-3', 5'-GAGGAGAAGCGAGAGGAGGT-3'), *Krt18* (5'-CGAGGCACTCAAGGAAGAAC-3', 5'-AATCTGGGCTTCCAGACCTT-3') , *Trp63*

(5’-AGCAGCACCAGCACCTACTT-3’, 5’-ATTCCTGAAGCAGGCTGAAA-3’), *Kit* (5’-AGTGCTTCCGTGACATTCAAC-3’, 5’-TGCCATTTATGAGCCTGTCGT-3’), *Elf5* (5’-CCAACGCATCCTTCTGTGAC-3’, 5’-AGGCAGGGTAGTAGTCTTCA-3’), *Esr1* (5’-CTGGACAGGAATCAAGGTAAA-3’, 5’-GAGGCACACAAACTCTTCTC-3’), *Pgr* (5’-CCACCTGTACTGCTTGAATAC-3’, 5’-CAACTGGGCAGCAATAACTTC-3’), *Prlr* (5’-ATAAAAGGATTTGATACTCATCTG-3’, 5’-GTCATCCACTTCCAAGAACTC-3’), *Snai1* (5’-ACACCTGTTTCACAGCAGTT-3’, 5’- TAGTTCTGGGAGACACATTG - 3’), *Snai2* (5’-GATGCCCAGTCTAGGAAATC-3’, 5’-CCCAGTGTGAGTTCTAATGT-3’), *Vim* (5’-CCAAGCAGGAGTCAAACGA-3’, 5’-TAAGGGCATCCACTTCACAG-3’), *Ki67* (5’-TCAATGTGCCTCGCAGTAAG-3’, 5’-GCATCTTTGGGGTTTTCTCA-3’), *Wap* (5’-AACATTGGTGTTCCGAAAGC-3’, 5’-GGTCGCTGGAGCATTCTATC-3’), *Csn2* (5’-TGCAGGCAGAGGATGTGCTCCAGGCT-3’, 5’-GGCCTGGGGCTGTGACTGGATGCT-3’) (Primer3v.0.4.0; http://bioinfo.ut.ee/primer3-0.4.0/primer3). *β-actin* (5’-AGGTGACAGCATTGCTTCTG-3’, 5’-GCTGCCTCAACACCTCAAC-3’) and *hprt* (5’-GCTGGTGAAAAGGACCTCT-3’, 5’-CACAGGACTAGAACACCTGC-3’) (Moreira Sousa et al., 2013) genes were used as internal controls. Fold changes were calculated using the ddCT method.

Statistical Analyses

Figure 1B
Data are from four independent cell sorting experiments: 5 mice per experiment
T test **p<0.01
Figure 1D
Data are from four independent cell sorting experiments: control: 5 mice per experiment, mutant: 5 mice per experiment
T test *p<0.05; **p<0.01
Figure 1F
Data are from four independent cell sorting experiments: control: 5 mice per experiment, mutant: 5 mice per experiment
T test **p<0.01; ***p<0.001
Figure 1G
Data are from four independent cell sorting experiments: control: 5 mice per experiment, mutant: 5 mice per experiment
T test *p<0.05
Figure 1H
Data are from four independent cell sorting experiments: control: 5 mice per experiment, mutant: 5 mice per experiment
T test ***p<0.001
Figure 1I
Data are from four independent cell sorting experiments: control: 5 mice per experiment, mutant: 5 mice per experiment
T test ***p<0.001

Figure 2A
Data are from four independent cell sorting experiments: control: 5 mice per experiment, mutant: 5 mice per experiment
T test *p<0.05; **p<0.01; ***p<0.001
Figure 2B
Data are from four independent cell sorting experiments: control: 5 mice per experiment, mutant: 5 mice per experiment
T test *p<0.05; **p<0.01; ***p<0.001
Figure 2D
Data are from: control: 4 mice; mutant: 4 mice
T test ***p<0.001
Figure 2E
Data are from: control: 4 mice; mutant: 4 mice
T test ***p<0.001
Figure 2G
Data are from three independent cell sorting experiments: control: 5 mice per experiment, mutant: 5 mice per experiment
T test *p<0.05; ***p<0.001
Figure 2H
Data are from three independent cell sorting experiments: control: 5 mice per experiment, mutant: 5 mice per experiment

T test ***p<0.001

Figure 3A
Data are from: control: 8 mice; mutant: 6 mice
T test *p<0.05
Figure 3B
Data are from: control: 5 mice; mutant: 5 mice
T test **p<0.01
Figure 3C
Data are from: control: 5 mice; mutant: 5 mice
T test ***p<0.01
Figure 3D
Data are from control: 3 mice; mutant: 3 mice
T test ***p<0.001

Figure 4D
Data are from: control: 10 mice (68 cells), mutant: 9 mice (62 cells)
T test ***p<0.001
Figure 4E
Data are from: control: 10 mice (43 cells), mutant: 9 mice (38 cells)
T test ***p<0.001
Figure 4F
Metaphase: Data are from: control: 10 mice (68 cells), mutant: 9 mice (62 cells)
Telophase: Data are from: control: 10 mice (43 cells), mutant: 9 mice (38 cells)
T test **p<0.01; ***p<0.001
Figure 4H
Data are from three independent experiments: si-Control: 64 cells, si-HTT1: 59 cells, si-dynein: 43 cells
ANOVA F[2,163] =7.018; p***<0.001
Fisher's PLSD:

	p-value
si-Control, si-HTT1	<0.001
si-Control, si-dynein	<0.001
si-HTT1, si-dynein	0.2488

Figure 4I
Data are from three independent experiments: si-Control: 98 cells, si-HTT1: 72 cells, si-dynein: 52 cells
ANOVA F[2,219] =37.60; p***<0.0001
Fisher's PLSD:

	p-value
si-Control, si-HTT1	<0.0001
si-Control, si-dynein	<0.0001
si-HTT1, si-dynein	0.2393

Figure 4K
Data are from five independent experiments: si-Control: 35 cells, si-HTT2: 32 cells, si-Control+HTTFL: 31 cells, si-HTT2+HTTFL: 30 cells, si-HTT2+HTTΔDYN: 32 cells

ANOVA F[4,155] =23.90; p***<0.0001
Fisher's PLSD:

	p-value
si-Control, si-HTT2	<0.0001
si-Control, si-Control+HTTFL	0.4907
si-Control, si-HTT2+HTTFL	0.5626
si-Control, si-HTT2+HTTΔDYN	<0.0001
si-HTT2, si-Control+HTTFL	<0.0001
si-HTT2, si-HTT2+HTTFL	<0.001
si-HTT2, si-HTT2+HTTΔDYN	0.2887
si-Control+HTTFL, si-HTT2+HTTFL	0.2177
si-Control+HTTFL, si-HTT2+HTTΔDYN	<0.0001
si-HTT2+HTTFL, si-HTT2+HTTΔDYN	<0.0001

Figure 4L
Data are from five independent experiments: si-Control+HTTFL: 34 cells, si-HTT2+HTTFL: 32 cells, si-HTT2+HTTΔDYN: 30 cells
ANOVA F[2,93] =11.80; p***<0.0001
Fisher's PLSD:

	p-value
si-Control+HTTFL, si-HTT2+HTTFL	0.3182
si-Control+HTTFL, si-HTT2+HTTΔDYN	<0.001
si-HTT2+HTTFL, si-HTT2+HTTΔDYN	<0.001

Figure 6D
Data are from three independent experiments:
Dynein: si-Control: 51 cells, si-HTT1: 53 cells
P150^{Glued}: si-Control: 36 cells, si-HTT1: 33 cells
NUMA: si-Control: 62 cells, si-HTT1: 57 cells
LGN: si-Control: 54 cells, si-HTT1: 40 cells
T test ***p<0.001
Figure 6G
Data are from three independent experiments: si-Control: 105 DHC-GFP cells and 88 LGN-GFP cells, si-HTT1: 92 DHC-GFP cells and 73 GFP-LGN cells
T test ***p<0.001

Figure 7D
Data are from three independent experiments: si-Control: 37 cells, si-HTT1: 39 cells
T test ***p<0.001
Figure 7E
Data are from three independent experiments: si-Control: 37 cells, si-HTT1: 39 cells
T test ***p<0.001
Figure 7H
Data are from three independent experiments:
P150^{Glued}: si-Control: 40 cells, si-kinesin-1: 40 cells
Dynein : si-Control: 39 cells, si-kinesin-1: 36 cells
NUMA: si-Control: 49 cells, si-kinesin-1: 52 cells

T test ***p<0.001

Figure 7I

Data are from three independent experiments: si-Control: 30 cells, si-kinesin-1: 33 cells
T test **p<0.01

Figures S1B and S1C

Data are from three independent cell sorting experiments: control: 5 mice per experiment, mutant: 5 mice per experiment
T test ***p<0.001

Figure S3D

Data are from three independent experiments: si-Control: 77 cells, si-HTT1: 75 cells
T test **p<0.01

Figure S3E

Data are from three independent experiments: si-Control: 108 cells, si-HTT1: 100 cells
T test **p<0.01; ***p<0.001

Figure S5D

P150^{Glued}: Data are from three independent experiments: si-Control: 32 cells, si-HTT2: 30 cells, si-HTT2+HTTFL: 30 cells, si-HTT2+HTTΔDYN: 30 cells
ANOVA F[3,8] =281.3; p***<0.0001
Fisher's PLSD:

	p-value
si-Control, si-HTT2	<0.0001
si-Control, si-HTT2+HTTFL	0.4892
si-Control, si-HTT2+HTTΔDYN	<0.0001
si-HTT2, si-HTT2+HTTFL	<0.0001
si-HTT2, si-HTT2+HTTΔDYN	0.2564
si-HTT2+HTTFL, si-HTT2+HTTΔDYN	<0.0001

Dynein: Data are from three independent experiments: si-Control: 34 cells, si-HTT2: 29 cells, si-HTT2+HTTFL: 30 cells, si-HTT2+HTTΔDYN: 30 cells
ANOVA F[3,8] =81.7; p***<0.0001
Fisher's PLSD:

	p-value
si-Control, si-HTT2	<0.0001
si-Control, si-HTT2+HTTFL	0.3492
si-Control, si-HTT2+HTTΔDYN	<0.0001
si-HTT2, si-HTT2+HTTFL	<0.0001
si-HTT2, si-HTT2+HTTΔDYN	0.1659
si-HTT2+HTTFL, si-HTT2+HTTΔDYN	<0.0001

NUMA: Data are from three independent experiments: si-Control: 37 cells, si-HTT2: 33 cells, si-HTT2+HTTFL: 33 cells, si-HTT2+HTTΔDYN: 31 cells
ANOVA F[3,8] =89.8; p***<0.0001
Fisher's PLSD:

	p-value
si-Control, si-HTT2	<0.0001

si-Control, si-HTT2+HTTFL	0.3377
si-Control, si-HTT2+HTTΔDYN	<0.0001
si-HTT2, si-HTT2+HTTFL	<0.0001
si-HTT2, si-HTT2+HTTΔDYN	0.4247
si-HTT2+HTTFL, si-HTT2+HTTΔDYN	<0.0001

LGN: Data are from three independent experiments: si-Control: 33 cells, si-HTT2: 33 cells, si-HTT2+HTTFL: 30 cells, si-HTT2+HTTΔDYN: 30 cells
ANOVA F[3,8] =158.7; p***<0.0001
Fisher's PLSD:

	p-value
si-Control, si-HTT2	<0.0001
si-Control, si-HTT2+HTTFL	0.1111
si-Control, si-HTT2+HTTΔDYN	<0.0001
si-HTT2, si-HTT2+HTTFL	<0.0001
si-HTT2, si-HTT2+HTTΔDYN	0.6054
si-HTT2+HTTFL, si-HTT2+HTTΔDYN	<0.0001

Figure S6B
Data are from three independent experiments: Control: 32 cells, Noco: 37 cells
T test **p<0.01
Figure S6D
Data are from three independent experiments:
P150^{Glued}: Control: 53 cells, Noco: 62 cells
Dynein: Control: 35 cells, Noco: 32 cells
NUMA: Control: 61 cells, Noco: 58 cells
LGN: Control: 51 cells, Noco: 45 cells
T test *p<0.05; **p<0.01; ***p<0.001
Figure S6E
Data are from three independent experiments:
P150^{Glued}: Control: 53 cells, Noco: 62 cells
Dynein: Control: 35 cells, Noco: 32 cells
NUMA: Control: 61 cells, Noco: 58 cells
LGN: Control: 51 cells, Noco: 45 cells
T test **p<0.01; ***p<0.001
Figure S6F
Data are from three independent experiments: Control: 61 cells, Noco: 45 cells
T test ***p<0.001

Supplemental References

Benn, C.L., Fox, H., and Bates, G.P. (2008). Optimisation of region-specific reference gene selection and relative gene expression analysis methods for pre-clinical trials of Huntington's disease. Mol Neurodegener *3*, 17.

Bolte, S., and Cordelieres, F.P. (2006). A guided tour into subcellular colocalization analysis in light microscopy. J Microsc *224*, 213-232.

Bouras, T., Pal, B., Vaillant, F., Harburg, G., Asselin-Labat, M.L., Oakes, S.R., Lindeman, G.J., and Visvader, J.E. (2008). Notch signaling regulates mammary stem cell function and luminal cell-fate commitment. Cell Stem Cell *3*, 429-441.

Dragatsis, I., Levine, M.S., and Zeitlin, S. (2000). Inactivation of Hdh in the brain and testis results in progressive neurodegeneration and sterility in mice. Nat Genet *26*, 300-306.

Godin, J.D., Colombo, K., Molina-Calavita, M., Keryer, G., Zala, D., Charrin, B.C., Dietrich, P., Volvert, M.L., Guillemot, F., Dragatsis, I.*, et al.* (2010). Huntingtin is required for mitotic spindle orientation and mammalian neurogenesis. Neuron *67*, 392-406.

Kaushik, R., Yu, F., Chia, W., Yang, X., and Bahri, S. (2003). Subcellular localization of LGN during mitosis: evidence for its cortical localization in mitotic cell culture systems and its requirement for normal cell cycle progression. Mol Biol Cell *14*, 3144-3155.

Kogata, N., and Howard, B.A. (2013). A whole-mount immunofluorescence protocol for three-dimensional imaging of the embryonic mammary primordium. J Mammary Gland Biol Neoplasia *18*, 227-231.

Lunkes, A., Lindenberg, K.S., Ben-Haiem, L., Weber, C., Devys, D., Landwehrmeyer, G.B., Mandel, J.L., and Trottier, Y. (2002). Proteases acting on mutant huntingtin generate cleaved products that differentially build up cytoplasmic and nuclear inclusions. Mol Cell *10*, 259-269.

Moreira Sousa, C., McGuire, J.R., Thion, M.S., Gentien, D., de la Grange, P., Tezenas du Montcel, S., Vincent-Salomon, A., Durr, A., and Humbert, S. (2013). The Huntington disease protein accelerates breast tumour development and metastasis through ErbB2/HER2 signalling. EMBO Mol Med *5*, 309-325.

Pardo, R., Molina-Calavita, M., Poizat, G., Keryer, G., Humbert, S., and Saudou, F. (2010). pARIS-htt: an optimised expression platform to study huntingtin reveals functional domains required for vesicular trafficking. Mol Brain *3*, 17.

Ramirez, A., Page, A., Gandarillas, A., Zanet, J., Pibre, S., Vidal, M., Tusell, L., Genesca, A., Whitaker, D.A., Melton, D.W.*, et al.* (2004). A keratin K5Cre transgenic line appropriate for tissue-specific or generalized Cre-mediated recombination. Genesis *39*, 52-57.

Soriano, P. (1999). Generalized lacZ expression with the ROSA26 Cre reporter strain. Nat Genet *21*, 70-71.

Soule, H.D., Maloney, T.M., Wolman, S.R., Peterson, W.D., Jr., Brenz, R., McGrath, C.M., Russo, J., Pauley, R.J., Jones, R.F., and Brooks, S.C. (1990). Isolation and characterization of a spontaneously immortalized human breast epithelial cell line, MCF-10. Cancer Res *50*, 6075-6086.

Steigemann, P., Wurzenberger, C., Schmitz, M.H., Held, M., Guizetti, J., Maar, S., and Gerlich, D.W. (2009). Aurora B-mediated abscission checkpoint protects against tetraploidization. Cell *136*, 473-484.

Stingl, J., Eirew, P., Ricketson, I., Shackleton, M., Vaillant, F., Choi, D., Li, H.I., and Eaves, C.J. (2006). Purification and unique properties of mammary epithelial stem cells. Nature *439*, 993-997.

Taddei, I., Deugnier, M.A., Faraldo, M.M., Petit, V., Bouvard, D., Medina, D., Fassler, R., Thiery, J.P., and Glukhova, M.A. (2008). Beta1 integrin deletion from the basal compartment of the mammary epithelium affects stem cells. Nat Cell Biol *10*, 716-722.

Vassilev, L.T., Tovar, C., Chen, S., Knezevic, D., Zhao, X., Sun, H., Heimbrook, D.C., and Chen, L. (2006). Selective small-molecule inhibitor reveals critical mitotic functions of human CDK1. Proc Natl Acad Sci U S A *103*, 10660-10665.